

# Dark Matter Substructure in Numerical Simulations: A Tale of Discreteness Noise, Runaway Instabilities, and Artificial Disruption

Frank C. van den Bosch<sup>1\*</sup>, Go Ogiya<sup>2</sup>,

<sup>1</sup>*Department of Astronomy, Yale University, PO. Box 208101, New Haven, CT 06520-8101*

<sup>2</sup>*Laboratoire Lagrange, Observatoire de la Côte d’Azur, CNRS, Blvd de l’Observatoire, CS 34229, F-06304 Nice cedex 4, France*

## ABSTRACT

To gain understanding of the complicated, non-linear and numerical processes associated with the tidal evolution of dark matter subhaloes in numerical simulation, we perform a large suite of idealized simulations that follow individual  $N$ -body subhaloes in a fixed, analytical host halo potential. By varying both physical and numerical parameters, we investigate under what conditions the subhaloes undergo disruption. We confirm the conclusions from our more analytical assessment in van den Bosch et al. that most disruption is numerical in origin; as long as a subhalo is resolved with sufficient mass and force resolution, a bound remnant survives. This implies that state-of-the-art cosmological simulations still suffer from significant overmerging. We demonstrate that this is mainly due to inadequate force-softening, which causes excessive mass loss and artificial tidal disruption. In addition, we show that subhaloes in  $N$ -body simulations are susceptible to a runaway instability triggered by the amplification of discreteness noise in the presence of a tidal field. These two processes conspire to put serious limitations on the reliability of dark matter substructure in state-of-the-art cosmological simulations. We present two criteria that can be used to assess whether individual subhaloes in cosmological simulations are reliable or not, and advocate that subhaloes that satisfy either of these two criteria be discarded from further analysis. We discuss the potential implications of this work for several areas in astrophysics.

**Key words:** instabilities — methods: numerical — galaxies: haloes — cosmology: dark matter

## 1 INTRODUCTION

Prior to 1997, numerical  $N$ -body simulations of structure formation in a cold dark matter (CDM) cosmology suffered from a serious ‘overmerging’ problem in that simulated CDM haloes revealed little to no substructure, in clear contrast with the wealth of ‘substructure’ (i.e., satellite galaxies) observed in galaxy groups and clusters. While some speculated that baryonic physics would resolve this problem (e.g., Frenk et al. 1988), others argued that it is a numerical artifact arising from insufficient mass and/or force resolution (e.g., Carlberg 1994; van Kampen 1995, 2000; Moore et al. 1996; Klypin et al. 1999a). Indeed, with increasing resolution the simulations started to reveal a wealth of substructure (e.g., Tormen et al. 1997; Brainerd et al. 1998; Moore et al. 1998), and by the close of the last mil-

lennium the ‘overmerging problem’ had been superseded by the ‘missing satellite problem’ (Klypin et al. 1999b; Moore et al. 1999). Over the years it has become clear that the latter is mainly a manifestation of poorly understood baryonic physics related to galaxy formation (see Bullock & Boylan-Kolchin 2017, for a comprehensive review), and the astrophysical community has become more and more confident that the  $N$ -body simulations make reliable predictions regarding the abundance and demographics of dark matter substructure (e.g., Ghigna et al. 1998; Klypin et al. 1999a; Diemand et al. 2004a; Gao et al. 2004; Kravtsov et al. 2004; Giocoli et al. 2008a, 2010). In particular, a number of resolution and comparison studies (e.g., Springel et al. 2008; Onions et al. 2012; Knebe et al. 2013; van den Bosch & Jiang 2016; Griffen et al. 2016) have

\* E-mail: frank.vandenbosch@yale.edu

shown that subhalo mass functions are converged<sup>1</sup> down to 50-100 particles per subhalo.

Does this mean that, in modern simulations, numerical overmerging only occurs when the subhalo has less than  $\sim 50$  particles? Subhalo disruption is still extremely prevalent in modern simulations, with inferred fractional disruption rates (at  $z = 0$ ) of  $\sim 13$  percent per Gyr (Diemand et al. 2004b; van den Bosch 2017). This implies that  $\sim 65$  (90) percent of all subhaloes accreted around  $z = 1$  ( $z = 2$ ) are disrupted by  $z = 0$  (Han et al. 2016; Jiang & van den Bosch 2016a). As discussed in van den Bosch (2017), roughly 20 percent of this disruption occurs above the mass resolution limit of 50 particles; in fact, the mass function of disrupting subhaloes is indistinguishable from that of the surviving population.

What is the dominant cause of this prevalent disruption of subhaloes in numerical simulations? In particular, is it artificial (numerical) or real (physical)? Based on the fact that simulations seem to yield consistent, converged results for the mass function (and spatial distribution) of subhaloes above a resolution limit of 50-100 particles, one is tempted to conclude that any disruption of subhaloes above this ‘resolution limit’ must be physical in origin (see Diemand et al. 2004b, for a detailed discussion). However, convergence is only a necessary, but not a sufficient condition to guarantee that the results are reliable. In addition, there is no consensus as to what physical mechanism dominates, with most studies arguing either for tidal heating or tidal stripping. We have therefore initiated a comprehensive study aimed at answering these questions. In van den Bosch et al. (2017, hereafter Paper I) we use both analytical estimates and idealized numerical simulations to investigate whether subhalo disruption is mainly physical, due to tidal heating and stripping, or numerical (i.e., artificial). We show that, in the absence of baryonic processes, the complete, physical disruption of CDM substructure is extremely rare, and that most disruption in numerical simulations therefore must be artificial. We discuss various processes that have been associated with numerical overmerging, and conclude that inadequate force-softening is the most likely culprit.

In this paper, we use a large suite of idealized numerical simulations and experiments to examine the tidal evolution and disruption of subhaloes in unprecedented detail. We confirm the conclusions from Paper I and demonstrate that state-of-the-art numerical  $N$ -body simulations indeed suffer from significant overmerging, mainly driven by inadequate force-softening. In addition, we show that subhaloes in  $N$ -body simulations are susceptible to a runaway instability which is triggered by the amplification of discreteness noise in the presence of a tidal field.

The main goal of this paper is to address the following questions:

- under what conditions does numerical disruption occur, and what causes it?
- what are the numerical requirements (i.e., number of

particles, softening length, time stepping, etc.) to properly resolve the tidal evolution of dark matter substructure.

Addressing these questions is facilitated by considering simplified settings, and we therefore resort to using idealized numerical simulations, in which we represent the subhalo by a  $N$ -body system, which we integrate in a static, analytical, external potential representing the host halo. We further simplify matters by predominantly considering circular orbits, and by focusing exclusively on dark matter (i.e., we ignore the potential impact of baryons). The goal of these idealized, numerical experiments is not to simulate realistic astrophysical systems, but rather to gain a physical understanding of the complicated, non-linear and numerical processes associated with the tidal stripping of dark matter subhaloes. Although the fraction of subhaloes/satellite galaxies on purely circular orbits is vanishingly small (e.g. Zentner et al. 2005; Khochfar & Burkert 2006; Wetzel 2011; van den Bosch 2017), and realistic host haloes are not static in that they respond dynamically to the presence of the subhalo, these idealizations have the advantage that they minimize the impact of tidal heating and dynamical friction, thereby allowing us to focus on the impact of tidal stripping. Most of the simulations presented below have been run for more than 60 Gyr, much longer than the age of the Universe. This stresses once more that we are striving to gain physical understanding, not necessarily to describe or model a realistic setting.

This paper is organized as follows. In §2 we describe the simulations, the initial conditions, and the treecodes and method used to run and analyze the simulations. §3 presents a case study of one of our idealized simulations, highlighting the typical tidal evolution of a dark matter subhalo. In §4 we assess the impact of four numerical parameters that control the accuracy of the simulations: the time step used to integrate the equations of motion, the tree opening angle used in the force calculation, the force softening length, and the actual number of particles used to simulate the subhalo in question. §5 presents a detailed convergence study, highlighting the impact of insufficient force softening and a discreteness-noise driven runaway instability. In §6 we examine under what conditions individual subhaloes in state-of-the-art cosmological simulations may be deemed ‘resolved’, §7 discusses the sensitivity of our results to various aspects of our (oversimplified) initial conditions, and §8 highlights some potential caveats of our study. Finally, §9 summarizes our results.

Throughout we adopt a Hubble parameter  $H_0 = 70 \text{ km s}^{-1} \text{ Mpc}^{-1}$ , which corresponds to a Hubble time of  $t_H = H_0^{-1} = 13.97 \text{ Gyr}$ .

## 2 METHODOLOGY

### 2.1 Initial Conditions

In this paper we simulate individual dark matter haloes (hereafter the ‘subhalo’ or ‘satellite’) orbiting in a fixed, external potential (hereafter the ‘host’ halo). Our goal is to investigate how much mass is stripped from the subhaloes and under what conditions the satellite disrupts (i.e., has no bound structure surviving).

Both the host halo and the *initial* (prior to the onset of

<sup>1</sup> A common practice with numerical simulations is to perform ‘convergence studies’ in which simulations are ran at different resolutions. Those results that are robust to an increase in resolution are deemed ‘converged’.

tidal stripping) subhalo are assumed to be spherical, and to have a NFW density profile

$$\rho(r) = \rho_s \left( \frac{r}{r_s} \right)^{-1} \left( 1 + \frac{r}{r_s} \right)^{-2}, \quad (1)$$

(Navarro et al. 1997), where  $r_s$  is the characteristic scale radius. We define the virial radius,  $r_{\text{vir}}$ , as the radius inside of which the average density is  $\Delta_{\text{vir}} = 97$  times the critical density for closure (Bryan & Norman 1998), and the halo concentration  $c \equiv r_{\text{vir}}/r_s$ . The virial mass of a halo,  $M_{\text{vir}}$ , is defined as the mass inside  $r_{\text{vir}}$ , while the virial velocity is defined as the circular velocity at the virial radius,  $V_{\text{vir}} = \sqrt{GM_{\text{vir}}/r_{\text{vir}}}$ . The crossing time for such a halo is

$$t_{\text{cross}} \equiv \frac{r_{\text{vir}}}{V_{\text{vir}}} = 2.006 \text{ Gyr}. \quad (2)$$

We generate initial conditions (ICs) assuming that the NFW subhalo has an isotropic velocity distribution, such that its distribution function (DF) depends only on energy, i.e.,  $f = f(E)$ . We use the method of Widrow (2000) to sample particles from the DF using the standard acceptance-rejection technique (Press et al. 1992; Kuijken & Dubinski 1994). We truncate the initial subhalo at a radius  $r_{\text{max}}$ , which is a free parameter of our model. Unless specifically stated otherwise, we adopt  $r_{\text{max}} = r_{\text{vir}}$ . Unfortunately, the DF that we use to generate the ICs is computed using the Eddington (1916) inversion equation, assuming that the halo extends to infinity. Consequently, unless  $r_{\text{max}} = \infty$  the initial system is not going to be in perfect equilibrium (see App. B of Paper I). Kazantzidis et al. (2004b) have suggested a way around this problem; following Springel & White (1999), they introduce an exponential cut-off for  $r > r_{\text{max}}$ , and compute  $f(E)$  from this modified density distribution using the Eddington equation. The cut-off sets in at  $r_{\text{max}}$  and exponentially decreases the density over a scale of  $r_{\text{decay}}$ , which is a free parameter that controls the sharpness of the transition. However, since we will embed our haloes in an external tidal field, with a corresponding tidal radius that lies well inside of  $r_{\text{max}}$ , there is little virtue to such an exponential cut-off, and to having a halo whose outskirts are in perfect equilibrium; even if the system were to be in perfect equilibrium in isolation, the moment we instantaneously introduce it to its tidal environment, it will no longer be in equilibrium.

Choi et al. (2007, 2009) try to account for the tidal field in their initial conditions, by truncating the halo at the radius beyond which subhalo particles on a circular orbit become unbound, and by using Eddington inversion to compute the corresponding DF. However, their method is also an approximation at best, as their simply cannot be a spherical, isotropic equilibrium solution for a system inside a tidal field.

The experiments conducted here correspond to idealized set-ups that one will never encounter in nature. In reality, subhaloes will already have been affected by the tidal field of the host halo well before it reaches the starting point of our simulation. If realism is the goal of the simulation, one has little choice but to simulate the system in its proper cosmological setting (i.e., run a cosmological simulation). The goal of the idealized experiments described here, though, is to gain a physical understanding of the complicated, non-linear and numerical processes associated with

the tidal stripping of dark matter subhaloes. Throughout the paper, we will comment on where the idealizations and approximations made may potentially impact the results and conclusions of our study. In particular, §7 presents a detailed discussion of how our ICs affect the outcome of the simulations.

## 2.2 Numerical Simulations

All simulations described in this paper have been carried out using one of two different  $N$ -body tree codes. The first is a modified version of the hierarchical  $N$ -body code **treecode**, written by Joshua Barnes with some improvements due to John Dubinski. **treecode** uses a Barnes & Hut (1986) oct-tree to compute accelerations based on a multi-pole expansion up to quadrupole order, and uses a straightforward second order leap-frog integration scheme to solve the equations of motion. Forces between particles are softened using a simple Plummer softening. The second code is specifically designed for graphic processing unit (GPU) clusters (Ogiya et al. 2013). Following the OT00 code developed by Nakasato et al. (2012), CPU cores construct oct-tree structures of  $N$ -body particles, while GPU cards compute gravitational accelerations through tree traversal. Ogiya et al. (2013) improved the algorithm of tree traversal proposed by Nakasato et al. (2012), increasing the speed of the GPU computations by a factor of 4. Hereafter, we refer this code as OT00+, which differs from **treecode** in that it (i) uses a second-order Runge-Kutta integrator and (ii) computes accelerations by defining the position of the cell as its centre of mass. Hence they are accurate up to dipole order. As we demonstrate in §3, despite these differences both codes yield results that are in excellent agreement; generally, we use the faster OT00+ whenever we use simulations with  $N_p > 10^6$ , and **treecode** otherwise.

Throughout we adopt model units in which the gravitational constant,  $G$ , the initial scale radius,  $r_{s,0}$ , and the initial virial mass of the subhalo,  $m_{s,0}$ , are all unity. With this choice, the initial virial velocity and crossing time of the subhalo are  $V_{\text{vir}} = 1/\sqrt{c_s}$  and  $t_{\text{cross}} = c_s^{3/2}$ , respectively, with  $c_s$  the subhalo's NFW concentration parameter. Unless stated otherwise, we restrict ourselves to subhaloes with  $c_s = 10$ , for which  $t_{\text{cross}} = 31.6$ . Based on Eq. (2) we thus have that a time interval of  $\Delta t = 1$  (model units) corresponds to 63.4 Myr. Throughout we adopt an NFW host halo of mass  $M_h = 1000m_{s,0}$ . In the  $\Lambda$ CDM cosmology, to good approximation, concentration scales with halo mass as  $c \propto M^{0.1}$  (e.g., Dutton & Macciò 2014). Hence, for a mass ratio of 1000, the ratio in concentration parameters is roughly 2, and we therefore adopt a concentration for the host halo of  $c_h = 5$ . Note that the host halo is always modeled as a fixed, external potential, while the subhalo is a live  $N$ -body system.

Unless specifically stated otherwise, we adopt a softening length given by

$$\varepsilon = 0.05 \left( \frac{N_p}{10^5} \right)^{-1/3}. \quad (3)$$

As discussed in §4.3, this is the optimal softening length for an NFW halo with  $N_p = 10^5$  and  $c_s = 10$  in isolation, while the scaling with  $N_p$  is motivated by van Kampen (2000). A detailed discussion as to how the choice of  $\varepsilon$  impacts the

**Table 1.** Fiducial Parameters

description	symbol	value
<b>Physical Parameters</b>		
initial mass of subhalo	$m_{s,0}$	1
mass of host halo	$M_h$	1000
concentration of subhalo	$c_s$	10
concentration of host halo	$c_h$	5
<b>Numerical Parameters</b>		
number of simulation particles	$N_p$	$10^5$
simulation time step	$\Delta t$	0.02
softening length (Plummer)	$\varepsilon$	0.05
tree opening angle	$\theta$	0.7

Parameters of our fiducial set of simulations expressed in model units for which  $G = m_{s,0} = r_{s,0} = 1$ .

simulations results is presented in §4.3. All simulations are run with a fixed time step of  $\Delta t = 0.02$ . As discussed in §4.1 this is an extremely conservative choice, which guarantees that we resolve the orbital time at the radius equal to the softening length with more than 30 steps. Finally, we adopt an opening angle for the force calculations equal to  $\theta = 0.7$ , which, as we demonstrate in §4.2 is also conservative, in that our results are extremely robust to changes in this parameter. For ease of reference, Table 1 summarizes the physical and numerical parameters of our ‘fiducial’ set of simulations.

### 2.3 Analysis

One of the main goals of this paper is to study how the bound mass of subhaloes evolve with time. We define

$$f_{\text{bound}}(t) \equiv \frac{m_s(t)}{m_{s,0}} = \frac{N_{\text{bound}}}{N_p} \quad (4)$$

Here  $m_s(t)$  is the bound mass of the subhalo at time  $t$ ,  $m_{s,0}(r)$  is the *initial* (prior to being exposed to the tidal field of the host halo) mass of the subhalo inside radius  $r$ ,  $N_{\text{bound}}$  is the number of bound particles at time  $t$ , and  $N_p$  is the total number of particles used in the simulation.

Determining  $f_{\text{bound}}(t)$  is non-trivial. We consider a particle  $i$  to be bound to the subhalo if its binding energy

$$E_i \equiv \frac{1}{2} m_i v_{\text{int},i}^2 - \sum_{j \neq i} \frac{G m_i m_j Q_j}{(|\mathbf{r}_j - \mathbf{r}_i|^2 + \varepsilon^2)^{1/2}} < 0. \quad (5)$$

Here  $Q_j$  is equal to 1 (0) if particle  $j$  is bound (unbound). Clearly, in order to be able to compute  $E_i$ , one first needs to know which are the bound particles. This can only be solved using an iterative scheme. Unfortunately, there is no unique way of performing this ‘unbinding’ operation, and this is where different analyses of the same simulation can cause significant differences (e.g., Muldrew et al. 2011; Knebe et al. 2011; Han et al. 2012, 2017). In our analysis we proceed as follows:

(i) We begin by making an initial guess for the boundness,  $Q_i$ , of each particle. At  $t = 0$  (ICs) we assume that each particle is bound ( $Q_i = 1 \forall i = 1, \dots, N_p$ ), while at later

times we assume that  $Q_i$  is the same as in the previous simulation output.

(ii) For each particle we compute  $E_i$  using Eq. (5). We update  $Q_i$  accordingly and compute the new, bound fraction  $f_{\text{bound}} = \frac{1}{N_p} \sum_i Q_i$ .

(iii) Compute the centre-of-mass position and velocity of the halo,  $\mathbf{r}_{\text{com}}$  and  $\mathbf{v}_{\text{com}}$ , as the average position and velocity of the  $N = \text{MAX}(N_{\text{min}}, f_{\text{com}} N_{\text{bound}})$  particles that are most bound. Here  $N_{\text{min}}$  and  $f_{\text{com}}$  are free parameters.

(iv) Update  $\mathbf{v}_i$  for each particle using the new centre-of-mass velocity.

(v) Go back to (ii) and iterate until the changes in  $\mathbf{r}_{\text{com}}$  and  $\mathbf{v}_{\text{com}}$  are smaller than  $10^{-4} r_{\text{vir}}$  and  $10^{-4} V_{\text{vir}}$ , respectively. This typically requires 3-10 iterations.

When computing the gravitational potential term of Eq. (5) we use a Barnes & Hut octree with the same opening angle,  $\theta$ , as in the simulation. We also adopt the same softening. Generally, smaller values of  $f_{\text{com}}$  results in a more noisy time-evolution of  $\mathbf{r}_{\text{com}}$  and  $\mathbf{v}_{\text{com}}$ , while for larger values of  $f_{\text{com}}$  it is more difficult to trace  $f_{\text{bound}}(t)$  when it becomes small. After careful testing, we obtain stable results for  $N_{\text{min}} = 10$  (we never use fewer than 10 particles to determine the centre-of-mass properties<sup>2</sup>) and  $f_{\text{com}} = 0.05$  (centre-of-mass properties are determined using the 5 percent most bound particles), which are the parameters we use throughout.

### 3 TIDAL STRIPPING ON CIRCULAR ORBITS

We start by considering the tidal evolution of NFW subhaloes on circular orbits in the (static) tidal field of an external host halo. The choice for circular orbits is motivated by the fact that in this case the tidal field strength is constant, thus minimizing the contribution from tidal shocking. As discussed in Paper I, this is, somewhat surprisingly, the most difficult case to treat analytically. Briefly, the main reason is that once some matter is stripped, the remaining remnant is no longer in virial equilibrium. It responds by re-virializing, which causes it to expand. This expansion, and the corresponding decrease in the tidal radius, causes additional matter to be stripped, bringing the system once again out of virial equilibrium. In a fixed tidal field (such as on the circular orbits considered here), this sequence of stripping and re-virialization basically continues *ad infinitum*. Since there is no robust, analytical theory for how to treat (re-)virialization, i.e., to compute how the density distribution of the subhalo responds to its outer layers being stripped<sup>3</sup>, it is not possible to develop a completely analytical treatment of tidal stripping. This is further exacerbated by the ill-defined nature of the tidal radius (see Paper I for a detailed discussion) and the self-friction briefly discussed in §3.2 below. As a consequence, we cannot validate the results from numerical simulations against an analytical test-case,

<sup>2</sup> Except when  $N_{\text{bound}} < 10$ , in which case we adopt  $N = N_{\text{bound}}$ .

<sup>3</sup> Several authors have attempted approximate treatments (e.g., Taylor & Babul 2001; Peñarrubia & Benson 2005; Pullen et al. 2014), but these approaches are crude at best, and still require calibration and validation based on numerical simulations.



and we are instead forced to validate the simulation results against each other, which is one of the main focuses of this paper.

Unless specifically stated otherwise, all subhaloes are initially truncated at their virial radius, and instantaneously introduced to the tidal field of the host halo (see §7 for discussion on the sensitivity to these initial conditions). We put the subhalo on a circular orbit of radius  $r_{\text{orb}}$ , and integrate the system for 50,000 timesteps of  $\Delta t = 0.02$  each, corresponding to a total integration time of  $\Delta t = 1000 = 63.4 \text{ Gyr}$  (roughly 4.5 times the age of the Universe). Note that  $r_{\text{orb}}$  is defined as the distance between the centres-of-mass of host and subhalo.

### 3.1 A Case Study

Before addressing how the evolution of the bound fraction,  $f_{\text{bound}}(t)$ , depends on the orbital radius and on various numerical parameters, we first examine one simulation in detail. Fig. 1 shows nine snapshots of one of our fiducial simulations (see Table 1), which follows the evolution of a subhalo on a circular orbit with  $r_{\text{orb}}/r_{\text{vir,h}} = 0.5$ . Each snapshot, the bound and unbound particles are indicated by red and black dots, respectively. The blue, dashed circle indicates the initial virial radius of the subhalo, which coincides with the initial truncation radius. The green, dashed circle marks the initial orbit on which the subhalo is placed. The upper left-hand corner of each panel indicates the time (in Gyr) and the bound fraction,  $f_{\text{bound}}$ , while the inset shows a zoom-in on the central region of the subhalo. The orbital time at  $r_{\text{orb}}/r_{\text{vir,h}} = 0.5$  is  $T_{\text{orb}} = 5.9 \text{ Gyr}$ , so that at the end of the simulation ( $t = 63.5 \text{ Gyr}$ ) the subhalo has almost completed 11 orbits around the centre of its host.

During the first orbital period, the subhalo loses about 68 percent of its mass, which increases to 75 percent after 10 Gyr. During the subsequent 53 Gyr, the subhalo only loses an additional  $\sim 13$  percent, while the tidally stripped material from the leading and trailing tidal arms is phase-mixed into two ring-like features. The surviving remnant, which after 60 Gyr still contains over 11,000 particles continues to orbit in between these two ‘rings’. Due to the perpetual sequence of stripping and re-virialization the subhalo continues to lose mass, even after 60 Gyr, albeit at a very slow rate.

Fig. 2 plots the density profiles (left-hand panel), circular velocity profiles (middle panel) and the radial velocity dispersion profiles (right-hand panels) of the bound subhalo in Fig. 1. Thin (green) and thick (black) lines show the profiles every 2.5 and 25 Gyr, respectively. Note how the density profile in the central region remains fairly constant over time, while the density profile in the outer regions becomes steeper and steeper as more and more matter is being stripped. After 50 Gyr, when the bound fraction has dropped to  $f_{\text{bound}} = 0.122$ , the mass enclosed within ten percent of the original scale radius has only been reduced by  $\sim 40$  percent, while the maximum (radial) velocity dispersion has dropped by  $\sim 35$  percent. Overall these results are in good agreement with previous studies (e.g., Hayashi et al. 2003; Peñarrubia et al. 2010).

The cautious reader may have noticed a pronounced, secondary ‘bump’ in the velocity dispersion profiles (right-hand panel of Fig. 2) at late times ( $t \gtrsim 10 \text{ Gyr}$ ). This is

due to material that is in the act of being stripped, with a small contribution due to transient phenomena. This is evident from Fig. 3, which shows a zoom-in on the subhalo at  $t = 33.3 \text{ Gyr}$ , where, for clarity, the central region with  $r < 2r_{\text{s},0}$  is cut-out. As in Fig. 1, red and black dots show the bound and unbound particles, respectively, while the blue-dashed circle marks the original virial radius of the subhalo. Note that the bound particles in the subhalo’s outskirts are distributed very anisotropically. There is a band of bound particles that fall roughly along the subhalo’s orbit (indicated by the green-dashed circle-segment), and two ‘shells’ of particles that are roughly parallel to this band. The former are particles that have recently been ‘stripped’ from the subhalo in that they are clearly tracing out a tidal stream. Formally, however, they are still bound to the subhalo, in the sense that they pass the boundness criterion adopted here (Eq. [5]). It are these particles, which typically become unbound within a small fraction of the subhalo’s orbital period, that are responsible for the secondary bump in the velocity dispersion profile. The two shells of ‘bound’ particles are made up of subhalo particles that were stripped at much earlier times, and that temporarily happen to pass the boundness criterion (Eq. [5]). We have verified that this transient bound population is small, and does not significantly impact our estimates of  $f_{\text{bound}}(t)$ .

### 3.2 Dynamical Self-Friction

Upon closer inspection, the insets in the lower panels of Fig. 1 show that, at late times, the bound remnant of the subhalo is orbiting inside of its original orbit (indicated by the green, dashed circle). This is a manifestation of ‘dynamical self-friction’ in which the stripped material exerts a force on the bound remnant, causing it to lose specific orbital energy to the tidally stripped material (see also Fujii et al. 2006; Fellhauer & Lin 2007). Note that dynamical friction due to the host halo is absent in our simulations, since the host halo is modeled using an analytical, static potential.

A detailed study of this dynamical self-friction will be presented in a forthcoming paper (van den Bosch & Go, in preparation). In the case of the simulations presented in this paper, which all have  $m_{\text{s},0}/M_{\text{h}} = 1/1000$ , the impact of dynamical self-friction is relatively weak, only affecting the orbital radius by a few percent at most. However, for larger mass ratios,  $m_{\text{s},0}/M_{\text{h}}$ , (not treated in this paper) we find the effect to be significantly larger, to the extent that it can cause the subhalo-remnant to lose most of its orbital energy and angular momentum in much less than a Hubble time. In general, dynamical self-friction transports the remnant towards the centre of the host halo, where the tidal field is stronger. This causes a decrease in the tidal radius and thus an enhancement in the mass loss rate. Hence, in addition to re-virialization, self-friction adds another positive feedback loop to the non-linear behavior of  $f_{\text{bound}}(t)$ , further inhibiting an analytical treatment.

### 3.3 Dependence on orbital radius

The colored lines in the upper left-hand panel of Fig. 4 show the bound fraction as function of time for subhaloes on different circular orbits, with  $r_{\text{orb}}/r_{\text{vir,h}}$  ranging from 1.0 (blue

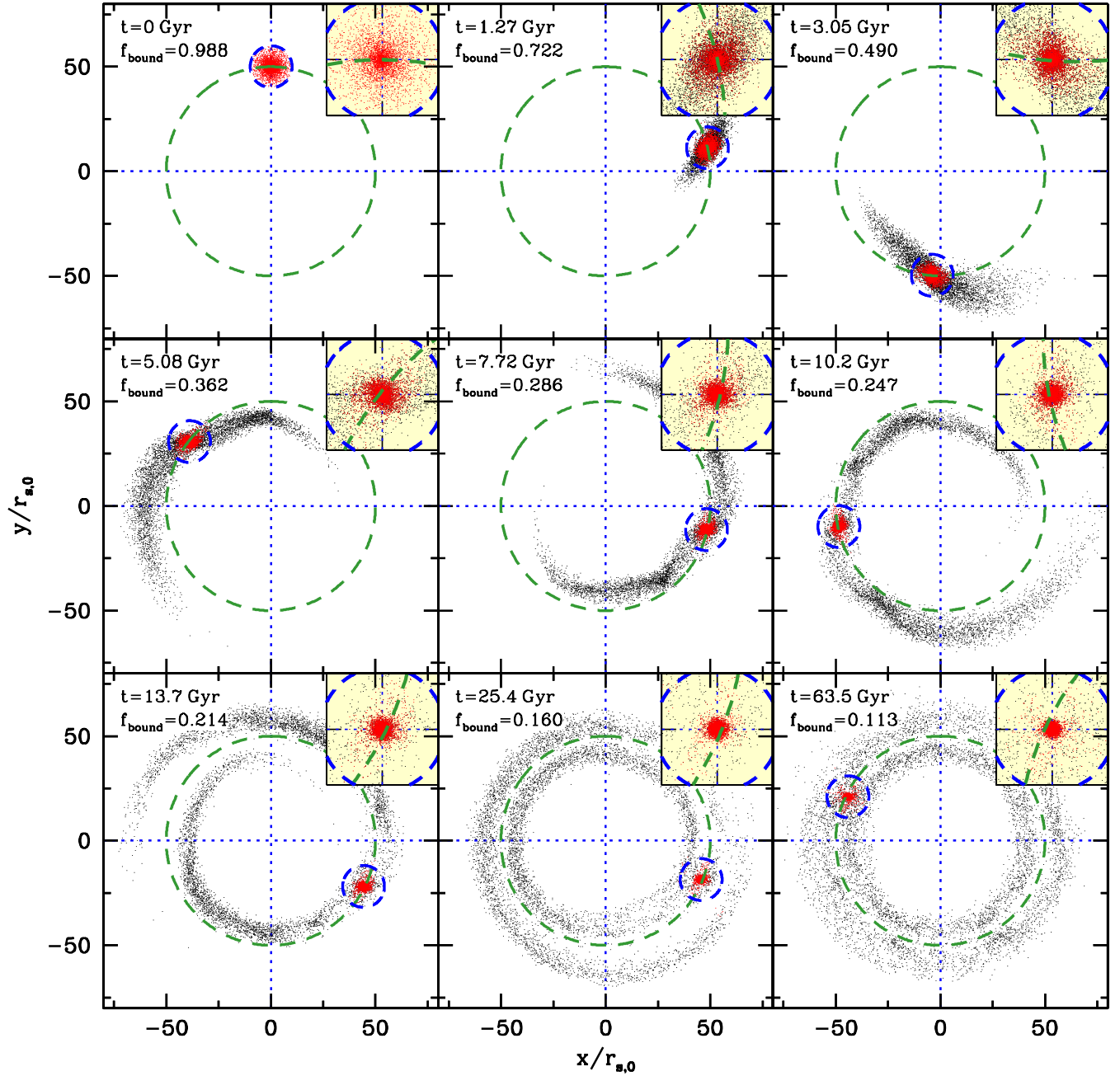


**Figure 1.** Snapshots of random subsets of subhalo particles in one of our fiducial simulations (see Table 1 for parameters), projected onto the orbital plane of the subhalo. Bound and unbound particles are indicated by red and black dots, respectively. The initial subhalo is truncated at its own virial radius, indicated by the blue, dashed circle, and reproduced in each panel for reference. The subhalo is placed on a circular orbit of radius  $r_{\text{orb}}/r_{\text{vir,h}} = 0.5$ , indicated by the green, dashed circle. Each panel indicates the time (in Gyr) and the bound fraction,  $f_{\text{bound}}$ , while the inset shows a zoom-in on the central region of the subhalo.

line) to 0.1 (red line). All these simulations are run using the fiducial parameters listed in Table 1. Solid and dotted lines correspond to simulations run with **treecode** and **OT00+**, respectively, and are in excellent agreement, indicating that our results are independent of which of the two codes we use. Note how all subhaloes survive for the full 60 Gyr of the simulation, except for the subhalo on the orbit with  $r_{\text{orb}}/r_{\text{vir,h}} = 0.1$ , which disrupts after  $\sim 13$  Gyr (corresponding to  $\sim 8.5$  orbits). Hence, based on these simulations one might be tempted to conclude that for the present set-

up ( $M_{\text{h}}/m_{\text{s},0} = 1000$ ,  $c_{\text{s}} = 10$ ,  $c_{\text{h}} = 5$ , and circular orbits), subhaloes disrupt when  $r_{\text{orb}}/r_{\text{vir,h}} \lesssim 0.15$ . However, as we demonstrate below, there are a number of numerical issues that have a strong impact on the results shown.

#### 4 NUMERICAL ISSUES

One of the main goals of this paper is to assess to what extent numerical  $N$ -body simulations are able to resolve the

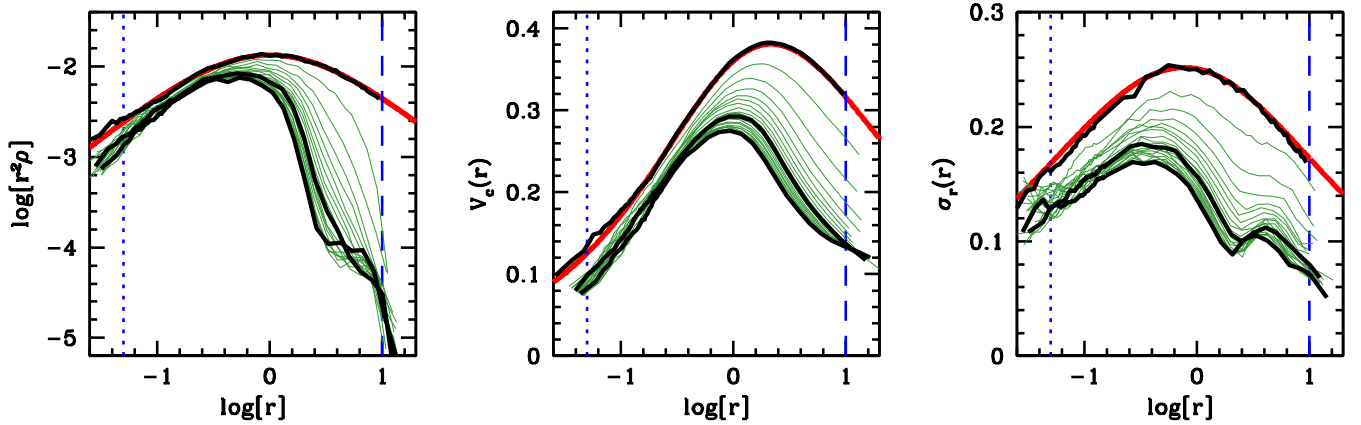


**Figure 2.** Density (left-hand panel), circular velocity (middle panel), and radial velocity dispersion (right-hand panel) profiles (in model units) of the bound subhalo particles in the same simulation as shown in Fig. 1. In the left-hand we plot  $\log[r^2\rho(r)]$ , rather than  $\log[\rho(r)]$  to better highlight small differences. Thin and thick lines show the profiles ever 2.5 and 25 Gyr, respectively, while the thick red lines indicate the analytical profiles. The vertical dotted and dashed lines mark the softening length and the initial virial radius, respectively.

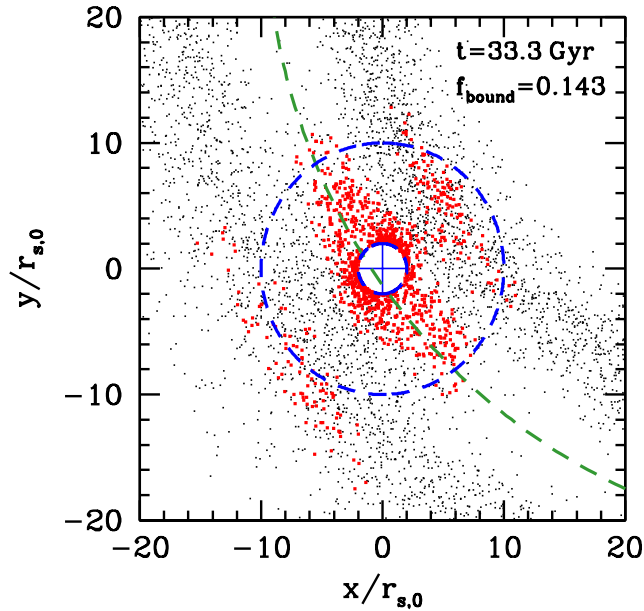


**Figure 3.** A snapshot of the subhalo in our fiducial simulation of Fig. 1 at  $t = 33.3$  Gyr. Bound and unbound particles are indicated by red and black dots, respectively. For enhanced clarity, we only show the particles in the subhalo outskirts ( $r > 2r_{s,0}$ ; the region inside of this is marked with a crosshair). As in Fig. 1 the blue and green dashed circles indicate the subhalo's original virial radius and orbit, respectively. Note the strongly anisotropic distribution of bound particles in the subhalo's outskirts (see text for discussion).

dynamics (i.e., accurately integrate the equations of motion) related to the tidal evolution of dark matter substructure. In this section we assess the impact of four numerical parameters that control the accuracy of such simulations: the time step,  $\Delta t$ , the tree opening angle,  $\theta$ , the softening length,  $\varepsilon$ , and the actual number of particles,  $N_p$ , used to simulate the system in question.

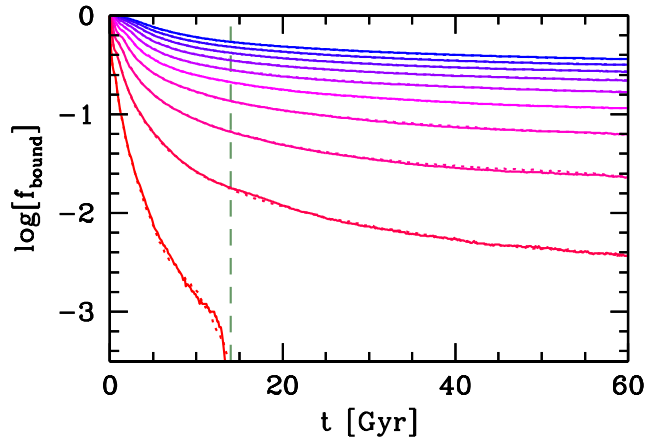


**Figure 4.** The bound fraction of subhaloes as function of time (in Gyr). Colors from blue to red correspond to  $r_{\text{orb}}/r_{\text{vir,h}} = 1.0, 0.9, \dots, 0.1$ , while solid and dotted lines (which almost lie on top of each other) correspond to simulations run with *treecode* and OT00+, respectively. The dashed, vertical line marks the Hubble time,  $t_H = 13.97$  Gyr. Note how the results from the two different simulation codes are in excellent agreement with each other, and how all subhaloes survive for  $> 60$  Gyr, except for the subhalo on a circular orbit with  $r_{\text{orb}} = 0.1r_{\text{vir,h}}$ , which disrupts after  $\sim 13$  Gyr.

#### 4.1 Timestepping

An important requirement for numerical  $N$ -body simulations is that the equations of motion are integrated accurately. In general, accuracy improves when using smaller time steps, but at the expense of increased computational cost. Modern cosmological simulations typically use adaptive time stepping, in which different criteria are used to determine the time step for each individual particle. However, adaptive time stepping is non-trivial and faces numerous challenges (see [Dehnen & Read 2011](#), for an overview). In this paper, we are conservative and only use simulations that employ a fixed time step,  $\Delta t$ , for all particles.

It is important to choose  $\Delta t$  sufficiently small, such that one accurately resolves the dynamics of the system. We re-

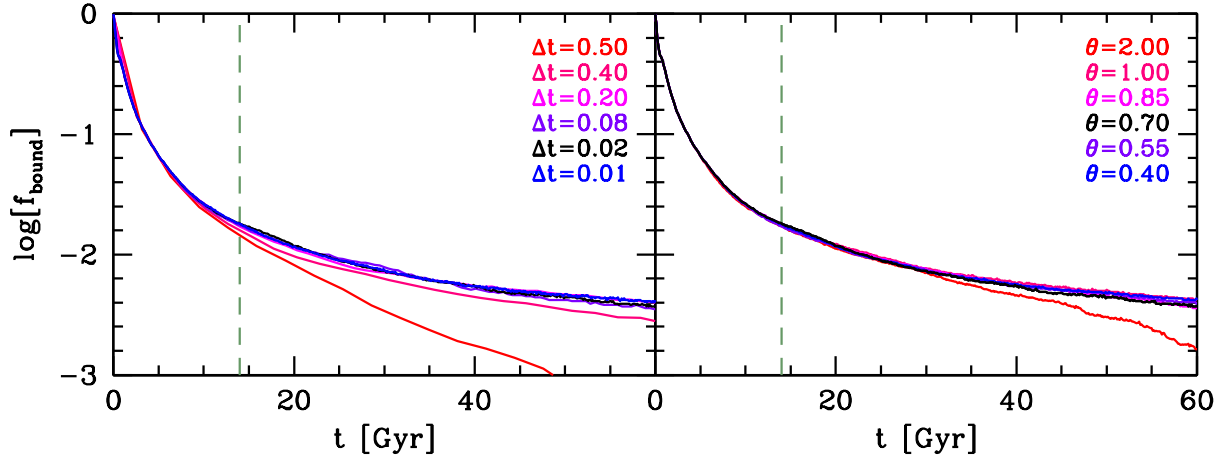


**Figure 5.** Impact of changing the time-step  $\Delta t$  (left-hand panel) and the opening angle  $\theta$  (right-hand panel) on the evolution of  $f_{\text{bound}}(t)$  for simulations with  $r_{\text{orb}}/r_{\text{vir,h}} = 0.2$ . All simulations use  $N_p = 10^5$  and a softening length  $\varepsilon = 0.05$ . The black line corresponds to our fiducial simulation, which has  $\theta = 0.7$  and  $\Delta t = 0.02$ , and the vertical dashed line indicates the Hubble time.

quire that  $\Delta t$  be significantly smaller than the *minimal* orbital time of the system, defined as the orbital time at the radius equal to the softening length,  $\tau_{\text{min}} = [3\pi/G\bar{\rho}(<\varepsilon)]^{1/2}$ , with  $\bar{\rho}(<\varepsilon)$  the average density enclosed by the softening length. In particular, we adopt  $\Delta t \leq \tau_{\text{min}}/30$ . The subhaloes simulated here have initial NFW density profiles with  $c = 10$ , for which

$$\Delta t < 0.256 \sqrt{\frac{\varepsilon^3}{\ln(1+\varepsilon) - \frac{\varepsilon}{1+\varepsilon}}}. \quad (6)$$

For the range of softening parameters considered in this paper ( $0.003 < \varepsilon < 0.25$ ), this implies  $0.02 < \Delta t < 0.21$ , with  $\Delta t = 0.08$  for our fiducial set-up ( $\varepsilon = 0.05$ , see §4.3).

In addition to properly resolving the relevant orbital times, the time step also impacts the accuracy of close encounters among particles. If the time step is too large, the resulting errors in the integration of such encounters causes an exacerbation of discreteness effects. As discussed in Power et al. (2003), achieving convergence down to a particular radius of a dark matter halo, for a particular duration of integration, puts a constraint on the ratio  $\Delta t/(N_p \varepsilon)$ ; for smaller ratios, the radius out to which the halo is properly resolved is smaller.

To test how our simulation results depend on the choice of time step, we have performed a series of simulations with different  $\Delta t$ . The left-hand panel of Fig. 5 shows the evolution of the bound mass fraction of our fiducial subhalo on a circular orbit with  $r_{\text{orb}} = 0.2r_{\text{vir,h}}$ . Different colors correspond to different time steps, as indicated, while all other parameters are kept fixed at their fiducial values ( $N_p = 10^5$ ,  $\varepsilon = 0.05$ , and  $\theta = 0.7$ ). The results are nicely converged as long as  $\Delta t \lesssim 0.4$ . Hence, based on the study by Power et al. (2003) we conclude that properly resolving the tidal evolution of dark matter substructure requires a time step

$$\Delta t < (\Delta t)_{\text{max}} = 0.4 \left( \frac{N_p}{10^5} \right) \left( \frac{\varepsilon}{0.05} \right) \quad (7)$$

We have repeated this test for other settings (other  $N_p$ ,  $\varepsilon$  and  $r_{\text{orb}}/r_{\text{vir,h}}$ ), and find that the above criterion accurately delineates the boundary between converged simulations and simulations in which the time step is too small. The latter

manifests in excessive mass loss and premature disruption, compared to simulations with  $\Delta t < (\Delta t)_{\text{max}}$ . In what follows we are conservative and always adopt a time step  $0.02 \leq \Delta t \leq (\Delta t)_{\text{max}}$ , which assures that accurate time integration of the equations of motion is not a limiting factor in any of the simulations presented below.

## 4.2 Force Accuracy

Both simulation codes used here are tree codes, which make use of the fact that the gravitational potential of a distant group of particles can be well-approximated by a low-order multipole expansion. In a tree code, the particles are therefore arranged in a hierarchical system of groups (cells) that form a tree structure. Forces are evaluated by ‘walking’ down the tree level by level, beginning with the top cell. At each level, a cell is added to an interaction list if it is distant enough for a force evaluation; if the cell is too close, it is ‘opened’ and the subcells (of which there are 8 in the case of an octree) are either used for force evaluation or opened further. A cell is opened, whenever  $d < l/\theta + \delta r$ . Here  $d$  is the distance between the particle in question and the centre-of-mass of the cell,  $\delta r$  is the distance between the centre of the cell and its centre-of-mass, and  $\theta$  is the opening angle, which controls the accuracy of the force calculation. Smaller  $\theta$  results in more accurate forces, but also increases computational cost.

Throughout we set  $\theta = 0.7$ , and we have verified through a number of tests that our results are extremely robust to changes in  $\theta$ . One such test is shown in the right-hand panel of Fig. 5, which plots the evolution of the bound mass fraction of our fiducial subhalo on a circular orbit with  $r_{\text{orb}} = 0.2r_{\text{vir,h}}$ . Different colors correspond to different values of  $\theta$ , as indicated, while all other parameters are kept fixed to their fiducial values (i.e.,  $N_p = 10^5$ ,  $\varepsilon = 0.05$ , and  $\Delta t = 0.02$ ). Note that decreasing  $\theta$  to 0.4 does not significantly change the results, indicating that our simulations are not limited by force accuracy. Only when we adopt extremely large values for the opening angle (i.e.,  $\theta \gtrsim 2$ ) do we notice significant departures from the converged (i.e., for



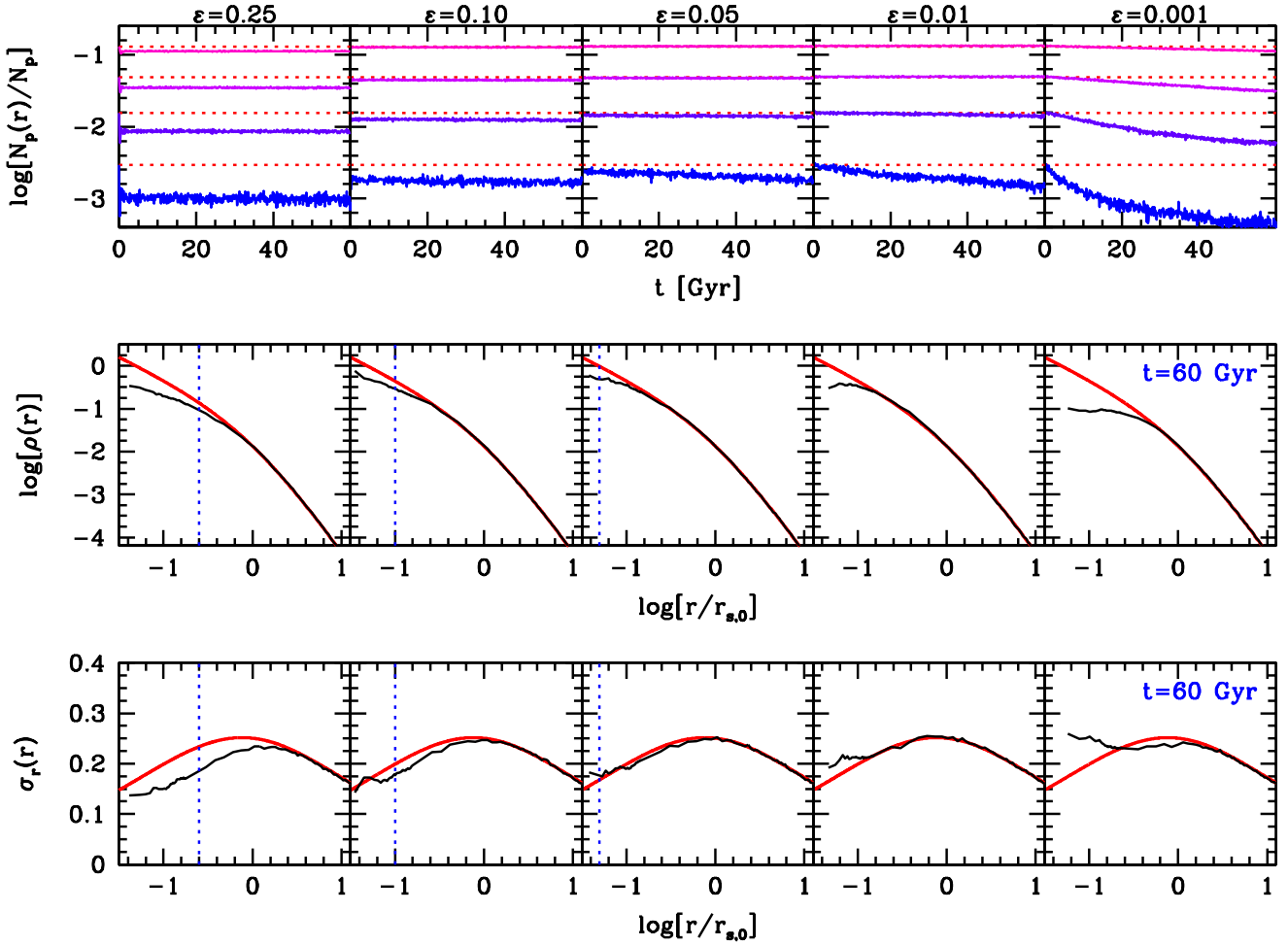


**Figure 6.** Impact of force softening on the evolution of an isolated NFW halo with  $N = 10^5$  particles inside its virial radius. Different columns correspond to different values of the softening length,  $\varepsilon$ , as indicated (in model units) at the top of each column. Upper panels show the normalized number of particles,  $N_p(r)/N_p$ , enclosed within fixed radii of  $r/r_{\text{vir}} = 0.01, 0.025, 0.05$  and  $1.0$  (different colors). The red, dotted, horizontal lines indicate the corresponding analytical predictions (i.e., in the absence of softening and in the limit of  $N_p \rightarrow \infty$ ). Panels in the middle and lower rows show the density profile,  $\rho(r)$ , and radial velocity dispersion profile,  $\sigma_r(r)$ , after  $t = 60$  Gyr, compared to their respective analytical profiles at  $t = 0$  (thick red lines). The vertical dashed lines indicate the softening length. See text for a detailed discussion.

much smaller  $\theta$ ) results. Throughout we are conservative and always adopt  $\theta = 0.7$ .

### 4.3 Force Softening

Typically, the choice for the softening length,  $\varepsilon$ , is a compromise between too much force *bias* (if  $\varepsilon$  is too large) and too much force *noise* (if  $\varepsilon$  is too small). Whereas the former results in a central potential well that is too shallow, the latter results in too many large-angle scattering events that create an artificial, isothermal core (e.g., Athanassoula et al. 2000; Dehnen 2001). Based on these considerations, Dehnen (2001) advocates that a Hernquist sphere (which has the same  $r^{-1}$  cusp as an NFW sphere), has an optimal softening length equal to  $\varepsilon_{\text{opt}}/r_{s,0} = 0.017 N_5^{-0.23}$ , where  $N_5 = N_p/10^5$ . Power et al. (2003) suggests picking a softening length for which the maximum stochastic acceleration caused by close encounters with individual particles,  $a_{\text{stoch}} \simeq Gm_p/\varepsilon^2$ , be smaller than the minimum mean-field acceleration in the halo,  $a_{\text{min}} \simeq GM_{\text{vir}}/r_{\text{vir}}^2$ . This im-

plies  $\varepsilon_{\text{opt}} \simeq r_{\text{vir}}/\sqrt{N_{\text{vir}}}$ , which translates to  $\varepsilon_{\text{opt}}/r_{s,0} \simeq 0.032 (c_s/10) N_5^{-1/2}$ . Note that Power et al. (2003) actually advocate using a softening that is a factor four times larger, but this is based on a trade-off between accuracy and minimizing the number of time steps required to reach convergence down to some radius. Since we are using relatively small simulations, minimizing the number of time steps is not a major concern to us, and we therefore opt for the smaller, more conservative optimal softening length. Finally, van Kampen (2000) advocates yet another criterion for the softening length, based on demanding (roughly) that the mean particle separation within the half-mass radius,  $r_h$ , be larger than the softening length. This implies  $\varepsilon_{\text{opt}} \propto 0.77 r_h N_p^{-1/3}$ . For an NFW halo, we find that to good approximation

$$\frac{r_h}{r_s} = 3.6 \times \left(\frac{c}{10}\right)^{0.63} \quad (8)$$

which implies  $\varepsilon_{\text{opt}}/r_{s,0} \simeq 0.060 (c_s/10)^{0.63} N_5^{-1/3}$ .

Based on the three criteria discussed above, the optimal

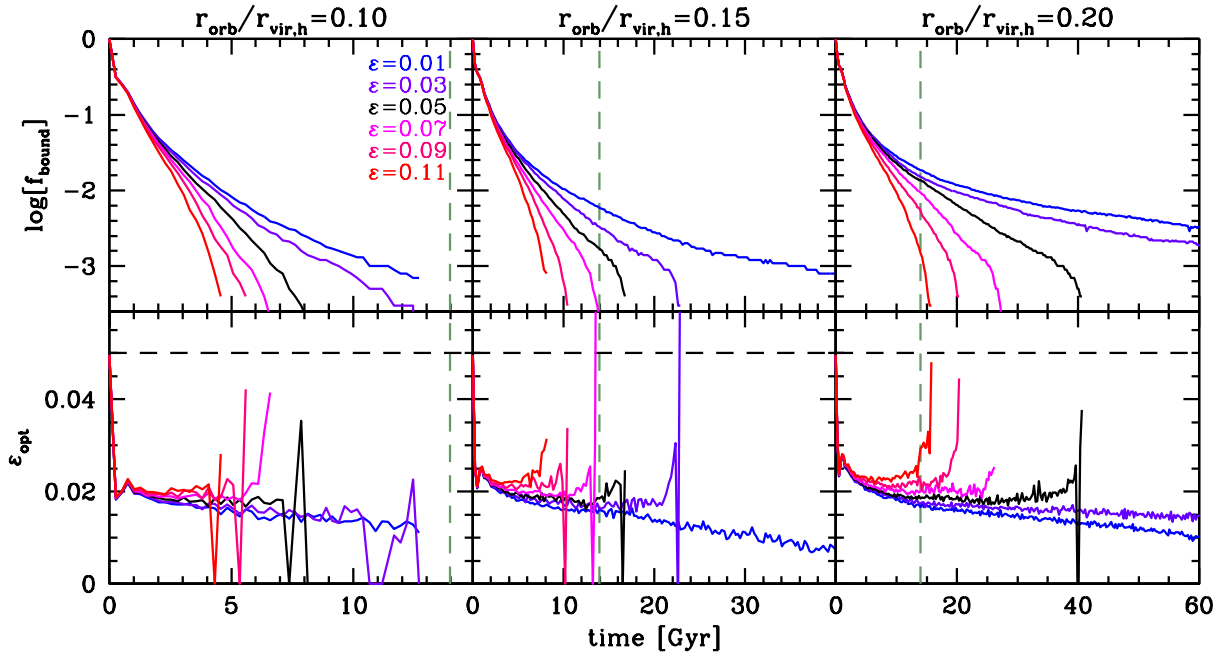


**Figure 7.** Impact of force softening on the evolution of a subhalo on a circular orbit in the tidal field of a fixed, analytical host halo. Top and bottom panels show the evolution of the bound mass fraction, and the value for the optimal softening length, respectively. The latter is defined as  $\varepsilon_{\text{opt}} = 0.05(r_h/r_{h,0})f_{\text{bound}}^{-1/3}$ . Lines of different color correspond to different values for the softening length, while different columns correspond to different orbital radii, as indicated. As in previous figures, the dashed, vertical lines indicate the Hubble time. Note how decreasing the softening length increases the bound mass fraction, causing the subhalo to survive longer.

softening length (in model units) for our fiducial simulations, which have  $N_5 = 1$  and  $c_s = 10$ , ranges from 0.02 to 0.06. To test this, we have performed a set of simulations of a NFW halo in isolation (i.e., no external tidal field), in which we only vary the softening parameter. Each simulation models the evolution of an NFW halo with concentration  $c = 10$  out to  $r_{\text{max}} = 10 r_{\text{vir}}$ . We simulate the system with  $N_p = 2.43 \times 10^5$  particles in total, such that the number of particles inside the virial radius equals  $10^5$ . We adopt our fiducial time step ( $\Delta t = 0.02$ ) and opening angle ( $\theta = 0.7$ ), and vary  $\varepsilon$  from 0.001 to 0.25. Each simulation is run for 50,000 time steps (corresponding to  $\sim 63$  Gyr). The results are shown in Fig. 6, where the upper panels show the normalized number of particles enclosed within fixed radii of  $r/r_{\text{vir}} = 0.01, 0.025, 0.05$  and  $1.0$  (different colors). The red, dotted, horizontal lines indicate the analytical predictions (i.e., in the absence of softening and in the limit of  $N_p \rightarrow \infty$ ). Panels in the middle and lower rows show the halo density profile and halo velocity dispersion profile,  $\sigma(r)$ , after  $t = 60$  Gyr, compared to their respective analytical profiles at  $t = 0$  (thick red lines).

As is evident, the results are ‘optimal’ when  $\varepsilon \simeq 0.05$ , in good agreement with the various  $\varepsilon_{\text{opt}}$ -criteria above. When  $\varepsilon$  is too large, the halo potential is overly softened, resulting in the density and velocity dispersion being too small at small radii. Since less dense systems are more easily stripped, we expect that in simulations with  $\varepsilon > \varepsilon_{\text{opt}}$  subhaloes experience enhanced stripping, and possibly artificial disruption. When  $\varepsilon$  is too small, the enclosed mass evolves with time due to two-body relaxation effects; energy is transported inwards, causing  $\sigma(r)$  to become isothermal in the centre, and the central density profile to evolve from a cusp into a

core. Hence, the naive expectation is that also for  $\varepsilon < \varepsilon_{\text{opt}}$  subhaloes experience enhanced tidal stripping and/or disruption.

To test how softening impacts the tidal evolution of subhaloes, we now put our fiducial NFW halo on a circular orbit within the (static) tidal field of our fiducial host halo ( $M_h = 1000, c_h = 5$ ). Fig. 7 show the results for three such orbits ( $r_{\text{orb}}/r_{\text{vir},h} = 0.1, 0.15$  and  $0.2$ , different columns), and for 6 different softening parameters each ( $\varepsilon = 0.01, 0.03, \dots, 0.11$ ; different colors). The upper panels show the evolution of the bound mass fraction with time. As expected, when  $\varepsilon > \varepsilon_{\text{opt}} \simeq 0.05$ , subhaloes experience enhanced stripping and disruption. However, contrary to expectations, when  $\varepsilon < \varepsilon_{\text{opt}}$  the simulated subhaloes have *larger* bound fractions and survive *longer*. The reason for this counter-intuitive behavior is that the optimal softening length scales with both the size of the system and the number of (bound) particles, both of which are evolving rapidly. The lower panels of Fig. 7 plot the evolution of the optimal softening length, based on the scaling relation advocated by van Kampen (2000);  $\varepsilon_{\text{opt}} = 0.05(r_h/r_{h,0})f_{\text{bound}}^{-1/3}$ , where  $r_{h,0}$  is the initial half-mass radius (prior to stripping). Note how  $\varepsilon_{\text{opt}}$  rapidly drops to  $\sim 0.02$ , after which it slowly decreases to 0.01. Most interestingly, all simulations show roughly the same behavior, independent of the actual softening length used. This suggests that the optimal softening length for subhaloes is smaller than that for isolated host haloes and that  $\varepsilon_{\text{opt}}$  may actually depend on the strength of the tidal field. We will come back to this issue in §5, but for now we conclude that changes in the softening parameter has a drastic impact on the tidal evolution of substructure in numerical simulations.

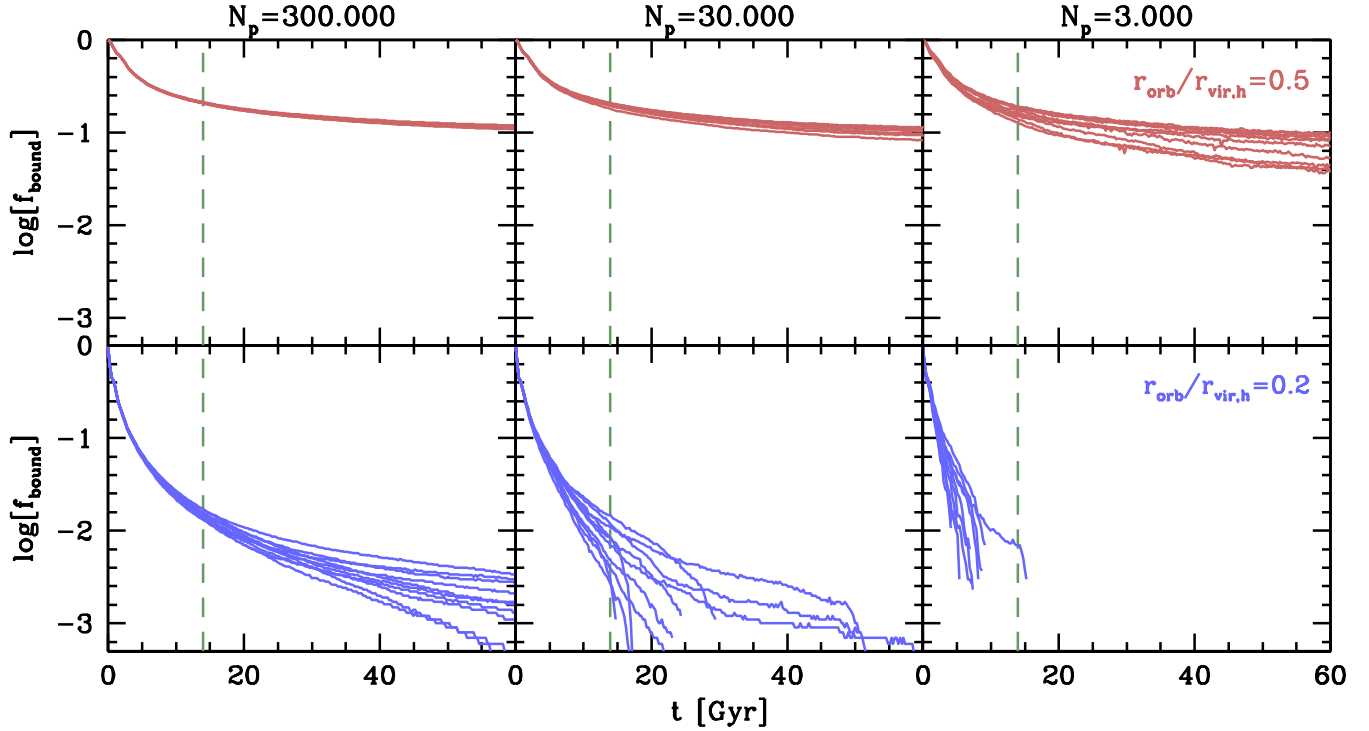


**Figure 8.** The bound mass fraction as function of time. Each panel shows 10 independent random realizations for a subhalo on a circular orbit with  $r_{\text{orb}}/r_{\text{vir,h}} = 0.5$  (upper panels) or  $r_{\text{orb}}/r_{\text{vir,h}} = 0.2$  (lower panels). Results are shown for simulations with  $N_p = 300,000$  (left-hand column),  $N_p = 30,000$  (middle column) and  $N_p = 3,000$  (right-hand column) particles, and a softening length of  $\varepsilon = 0.05(N_p/10^5)^{-1/3}$ . The vertical dashed line indicates the Hubble time. Note how the variance among the different random realizations increases with time due to a discreteness-driven runaway instability.

#### 4.4 Discreteness Noise

When using a fairly limited number of particles to sample the DF, one is subject to discreteness noise. The corresponding Poisson fluctuations in the density and potential of the subhalo impact the dynamics. For instance, they cause collective relaxation (a numerical artefact), which is reminiscent of violent relaxation (a physical process), and which, under certain conditions, can dominate over two-body relaxation (Weinberg 1993). To gauge the impact of discreteness noise on the evolution of  $f_{\text{bound}}(t)$ , we have run a large number of simulations using different random realizations when setting up the ICs. The findings are summarized in Fig. 8 which plots the mass fraction as function of time. Results are shown for two different orbits,  $r_{\text{orb}}/r_{\text{vir,h}} = 0.5$  (upper panels) and  $r_{\text{orb}}/r_{\text{vir,h}} = 0.2$  (lower panels), and for three different mass resolutions,  $N_p = 300,000$  (left-hand panels),  $N_p = 30,000$  (middle panels) and  $N_p = 3,000$  (right-hand panels). When changing the number of particles, we also change the softening length according to  $\varepsilon = 0.05(N_p/10^5)^{-1/3}$  (see §2.2).

Each panel shows the results for ten different simulations that only differ in the random realization of the ICs. In the absence of discreteness noise these ten realizations should yield exactly identical results. In practice, however, the simulations display diverging behavior in  $f_{\text{bound}}(t)$ , which becomes more pronounced for smaller  $N_p$  and/or smaller  $r_{\text{orb}}/r_{\text{vir,h}}$ . In some cases, the divergence is dramatic. For example, in the case with  $r_{\text{orb}}/r_{\text{vir,h}} = 0.2$  and  $N_p = 30,000$  some subhaloes survive for  $> 60$  Gyr, while oth-

ers disrupt in just under a Hubble time. When  $N_p = 3,000$  the subhalo always disrupts, but with a disruption time that varies from  $\sim 5$  Gyr to  $\sim 15$  Gyr. Even with  $N_p = 300,000$ , the discreteness noise results in a simulation-to-simulation variance in  $f_{\text{bound}}$  after 60 Gyr with a standard deviation of  $\sim 0.4$  dex.

We can characterize the sensitivity to this discreteness noise using the variance,  $\sigma_{\log f}$ , in  $\log(f_{\text{bound}})$  among these sets of simulations. Fig. 9 plots the logarithm of  $\sigma_{\log f}$  in the  $r_{\text{orb}}/r_{\text{vir,h}} = 0.2$  simulations as a function of  $\log(N_p)$ . Results are shown for two epochs, 1 and 5 Gyrs after the start of the simulations. As expected, the standard deviation increases with time and with decreasing number of particles. The red-dotted lines in Fig. 9 correspond to

$$\sigma_{\log f} \propto N_p^{-1/2} t, \quad (9)$$

anchored to the standard deviation at  $\log N_p = 5$  and  $t = 1$  Gyr. Clearly, this scaling, which is in line with simple predictions for discreteness noise, provides a fairly good description of the simulation results. However, at later times, and small  $N_p$ , the standard deviation is larger than predicted by Eq. (9). We have performed a number of tests, mainly varying softening lengths, which suggest that this deviation arises because for small  $N_p$  the dynamics at later times is strongly influenced by force bias arising from poor softening: when using smaller softening lengths the simulation results more closely follow the scaling relation of Eq. (9). We have also repeated the above experiments in which we first run the haloes in isolation for 10 Gyr, allowing them to virialize before we introduce them to the tidal field of

the host halo. The resulting divergence is indistinguishable from that in the runs shown above. This indicates that the diverging behavior among the various realizations is due to discreteness rather than due to the initial conditions not being in perfect equilibrium (see §7 for more details).

Although the simulations roughly obey the scaling relation of Eq. (9), we emphasize that its *normalization* depends on a number of physical parameters such as the tidal field strength (e.g.,  $r_{\text{orb}}$ ,  $M_h$ ,  $c_h$ ) and the structural parameters of the subhalo (i.e.,  $c_s$ ). Typically, the impact of discreteness noise on the evolution of the subhalo increases with the strength of the tidal field. This is evident from comparing the upper and lower panels of Fig. 8, which show a much stronger divergence in  $f_{\text{bound}}$  for smaller  $r_{\text{orb}}$ . In addition, we have run the same ten realizations in isolation (i.e., in the absence of an external tidal field), in which case we find no significant divergence in their evolution.

#### 4.5 A Discreteness-Driven Run-Away Instability

In order to understand the origin of the divergence in the bound mass fractions, it is useful to envision the tidal radius as characterizing a semi-permeable surface; once a particle crosses this surface it will be stripped off. Due to discreteness noise, the number of particles that cross this tidal surface during any time interval  $\Delta t$  is subject to Poisson fluctuations. Now consider a high fluctuation, i.e., a time interval during which the mass loss rate is higher than average. As a consequence, the remaining remnant experiences more re-virialization than average, which results in its size expanding more than average. As a result, the tidal radius shrinks more than average, and the next time step  $\Delta t$  the subhalo is therefore more likely to once again lose more mass than on average. Hence, discreteness noise gives rise to a run-away instability that is triggered by the presence of a tidal field. This is an important, and potentially worrying result, as it implies that the evolution of subhaloes in cosmological simulations is likely to be severely impacted by discreteness noise. As the results shown here suggest, this discreteness noise can trigger artificial disruption of subhaloes even when they are still resolved with thousands of particles.

## 5 TOWARDS CONVERGENCE

In the previous section we have demonstrated that our simulation results are subject to a run-away instability due to discreteness noise and extremely sensitive to the softening length used, whose optimal value appears to depend on the strength of the tidal field. This begs the question; what is the correct tidal evolution of substructure and what are the numerical requirements to properly track such evolution in  $N$ -body simulations? Unfortunately, as discussed in §3 and Paper I, there is no analytical answer, and we therefore have to rely on numerical simulations. We now undertake a detailed resolution study, in which we increase  $N_p$  and vary  $\epsilon$  until we reach a ‘converged’  $f_{\text{bound}}(t)$ . Here converged means that (i) no significant changes occur when  $N_p$  is increased

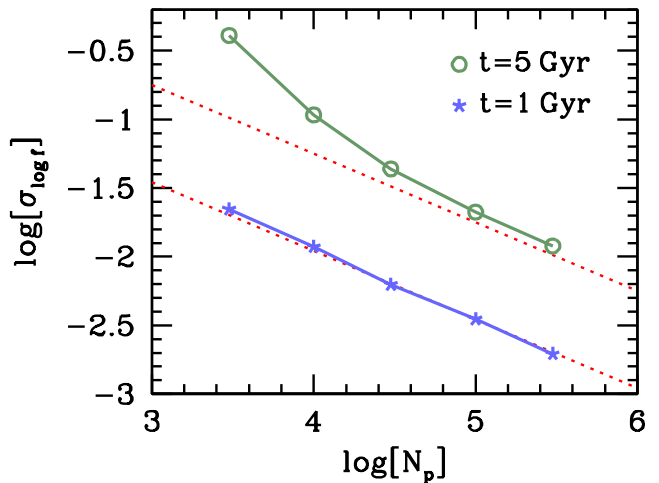


**Figure 9.** The standard deviation in  $\log f_{\text{bound}}$  among 10 different realizations as a function of the logarithm of the number of particles used in the simulations. Results are shown at two epochs, 1 and 5 Gyrs, after the start of the simulations, as indicated. The red, dotted lines correspond to  $\sigma_{\log f} \propto N_p^{-1/2} t$ , and are shown for comparison. Note that increasing  $N_p$  results in a clear reduction of the standard deviation among different realizations, indicating that the variance is mainly due to discreteness noise. All these results are for simulations with  $r_{\text{orb}}/r_{\text{vir,h}} = 0.2$  and adopt a softening length of  $\epsilon = 0.05 (N_p/10^5)^{-1/3}$ .

further<sup>4</sup>, and (ii) the standard deviation in  $f_{\text{bound}}$  after one Hubble time is sufficiently small (i.e.,  $\sigma_{\log f} \lesssim 0.05$ ).

We start by considering a circular orbit with  $r_{\text{orb}}/r_{\text{vir,h}} = 0.1$ . As shown in van den Bosch (2017), this is the typical radius at which dark matter subhaloes in the Bolshoi simulation (Klypin et al. 2011) undergo disruption, and by focusing on this orbit we therefore hope to gain some understanding as to whether such disruption is real (physical) or artificial (numerical). The results of our convergence study for this orbit are shown in Fig. 10, which summarizes the results of over 200 simulations with different  $N_p$  and  $\epsilon$ ; all other parameters are kept fixed at their fiducial values. Each panel shows the evolution of the bound fraction as inferred from 10 random realizations (blue curves) with the same  $N_p$  and  $\epsilon$ . The red curve indicates the corresponding average of  $\log[f_{\text{bound}}]$ , while the thick solid curve indicates the evolution of the bound fraction for the ‘converged’ result, which in this case has  $N_p = 10^7$  and  $\epsilon = 0.003$ . From top to bottom  $N_p$  decreases from  $10^6$  to  $3 \times 10^4$ , while from left to right  $\epsilon$  increases from 0.003 to 0.1, as indicated. The vertical, dashed line marks the Hubble time.

The results in the upper-left corner ( $N_p = 10^6$  and  $\epsilon = 0.003$ ) are in good agreement with our converged results, but has  $\sigma_{\log f} \simeq 0.1$  (i.e., there is a 0.1dex uncertainty on the surviving halo mass) after one Hubble time. Increasing the softening length while keeping the number of particles fixed at  $N_p = 10^6$  causes a systematic deviation from the converged (‘true’) results, the amplitude of which clearly increases with  $\epsilon$ ; For  $\epsilon = 0.03$ , the subhaloes disrupt after  $(9 \pm 1)$  Gyr, while with  $\epsilon = 0.1$  the subhaloes disrupt after only  $\sim 5$  Gyr. If instead we keep  $\epsilon = 0.003$  and decrease  $N_p$ ,

<sup>4</sup> while decreasing the softening accordingly, see §4.3



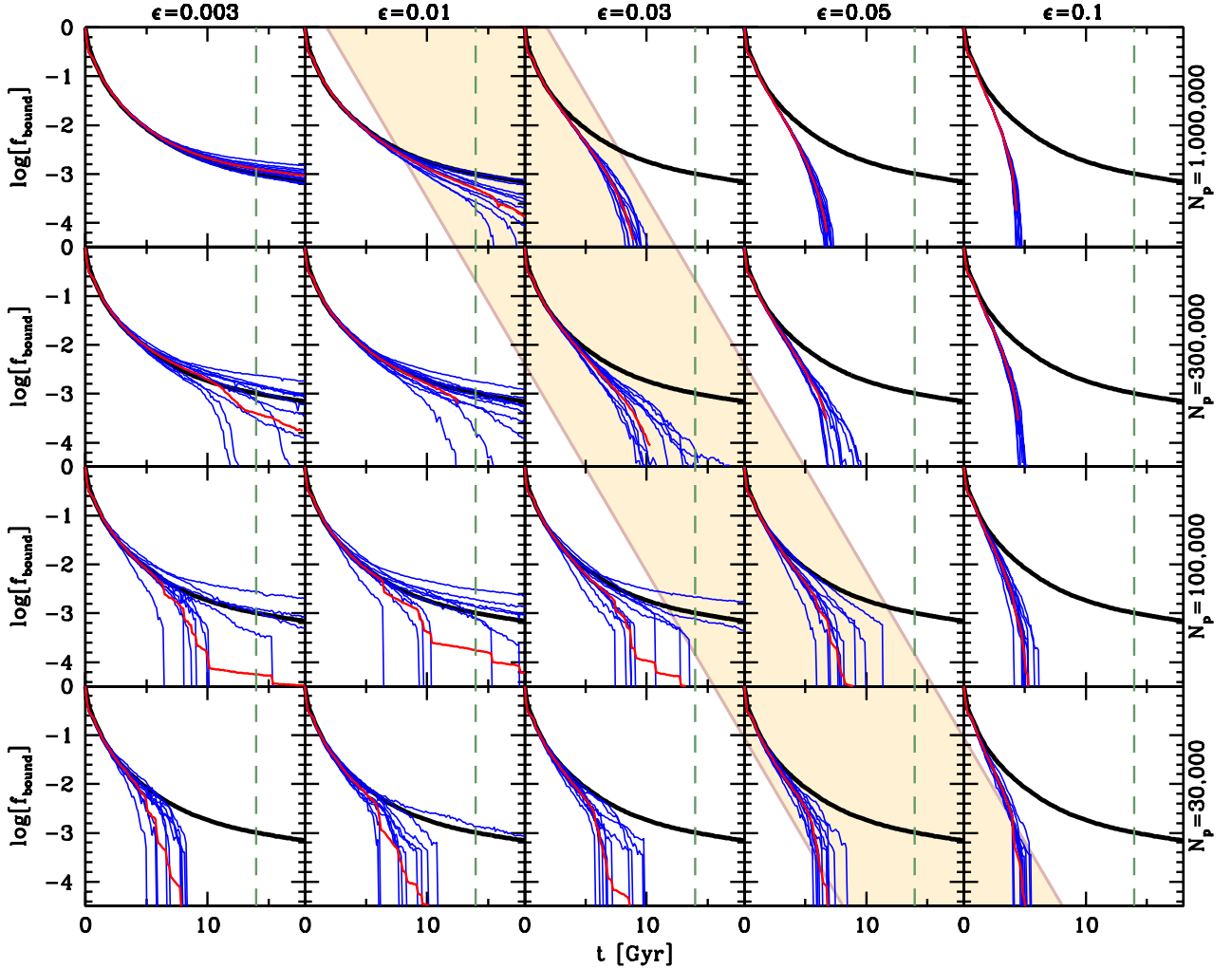


**Figure 10.** Bound fraction as function of time for simulations with different  $N_p$  (different rows) and different softening length,  $\epsilon$  (different columns). All simulations follow the evolution of a subhalo with  $c_s = 10$  on a circular orbit with  $r_{\text{orb}}/r_{\text{vir,h}} = 0.1$  in a host halo with  $M_h = 1000m_{s,0}$  and  $c_h = 5$ . The solid, black line indicates the converged results, based on a simulation with  $N_p = 10^7$  and  $\epsilon = 0.003$ . Blue lines indicate the results from 10 simulations, that only differ in the random realization of the initial conditions, while the red line indicates their average. Vertical, dashed lines marks the Hubble time, while the yellow shaded band indicates the typical  $(N_p, \epsilon)$  with which subhaloes are resolved in state-of-the-art cosmological simulations (the width of the band matches the width of the panels, and does not have a physical meaning). See text for a detailed discussion.

the impact of discreteness noise becomes more and more apparent. With  $N_p = 10^5$  the standard deviation  $\sigma_{\log f}$  already reaches 0.1dex after only  $\sim 4\text{Gyr}$ .

Clearly, properly resolving the dynamics associated with the tidal evolution of substructure at 10 percent of the virial radius of the host halo requires extremely high mass resolution (i.e., large  $N_p$ ) as well as superb force resolution (i.e., small  $\epsilon$ ). To compare this with the typical mass and force resolutions used in state-of-the-art cosmological simulations, consider the Millennium simulation (Springel et al. 2005), which has a particle mass  $m_p = 8.6 \times 10^8 h^{-1} M_\odot$  and a softening length of  $5h^{-1}$  kpc comoving (Plummer equivalent). Using the concentration-mass relation of Neto et al. (2007), according to which  $c_{200} = 5.26(M_{200}/10^{14} h^{-1} M_\odot)^{-0.1}$ , this implies that haloes with  $N_{200}$  particles within the radius that encloses a density equal to 200 times the critical density are resolved with a softening

length, in units of the NFW scale radius, given by

$$\frac{\epsilon}{r_s} = 0.037 \left( \frac{N_{200}}{10^5} \right)^{-0.43}, \quad (10)$$

where we have used that  $r_s = r_{200}/c_{200}$  and  $r_{200} \propto M_{200}^{1/3} \propto N_{200}^{1/3}$ . The yellow-shaded band in Fig. 10 roughly reflects this scaling. It shows that the Millennium simulation is unable to properly resolve the dynamical evolution of subhaloes on circular orbits with  $r_{\text{orb}}/r_{\text{vir,h}} \simeq 0.1$ ; they are subject to the discreteness driven run-away instability identified in §4.4, and they experience artificial disruption due to a softening length that is too large.

It is important to emphasize that this is not specific to the Millennium simulation. In fact, most state-of-the-art cosmological simulations resolve subhaloes with force softening that roughly follow the scaling reflected by the yellow-shaded band. The reason is that many simulations adopt the scaling relation of Power et al. (2003) to pick their soft-

ening length. According to that relation,  $\varepsilon \propto N_p^{-0.5}$ , which is very similar to the scaling of Eq. (10). In other words, simulations of different mass resolution typically scale their softening parameter such that subhaloes of a given physical mass are resolved with a  $N_p$  and  $\varepsilon$  that fall (roughly) along the yellow-shaded band. Along this band, though, results look fairly similar, indicating that convergence is extremely slow. This implies that simply improving the mass and force resolution of numerical simulations, following the Power et al. (2003) scaling relations, may give results that appear converged, but that in reality continue to suffer from numerical artifacts. As we discuss in §9 below, this may have profound implications for numerous areas of astrophysics.

Fig. 11 shows the same results, but now for a circular orbit with  $r_{\text{orb}}/r_{\text{vir,h}} = 0.2$ . As in Fig. 10, the yellow-shaded band corresponds to the scaling relation of Eq. (10) and therefore indicates the typical  $(N_p, \varepsilon)$  with which haloes are resolved in typical state-of-the-art cosmological simulations. Clearly, the requirements to properly resolve the dynamics along this orbit are much weaker than along an orbit with  $r_{\text{orb}}/r_{\text{vir,h}} = 0.1$ : typically the dynamics are properly converged for the duration of a Hubble time as long as  $N_p \gtrsim 10^5$  and the softening length roughly follows the scaling of Power et al. (2003). In fact, as long as  $N_p \gtrsim 10^5$  there is quite a large range in softening values for which the results are indistinguishable. Note also, though, that for  $N_p < 10^4$  the subhaloes experience artificial disruption and are subject to severe discreteness noise.

### 5.1 Timescales

To make the results in Figs. 10 and 11 more quantitative, we compute, for each  $(N_p, \varepsilon, r_{\text{orb}}/r_{\text{vir,h}})$  two time scales. The first is the ‘systematic’ time,  $T_{\text{sys}}$ , which we define as the time it takes for the average of the 10 random realizations (the red curves in Figs. 10 and 11) to deviate more than 0.1dex from the converged results (the thick black curves). Note that this deviation is always in the sense of too much mass loss, which in many cases results in artificial disruption. In addition, we also define the discreteness time,  $T_{\text{dis}}$ , as the time it takes for the standard deviation among the 10 random realizations to become 0.1dex. The results are shown in Fig. 12, where the upper and lower panels corresponds to  $r_{\text{orb}}/r_{\text{vir,h}} = 0.1$  and 0.2, respectively. The left column shows for each  $(N_p, \varepsilon)$  whether simulations with these parameters suffer from systematic errors ( $T_{\text{sys}} < \text{MIN}[T_{\text{dis}}, t_H]$ ; solid red circle), from discreteness noise ( $T_{\text{dis}} < \text{MIN}[T_{\text{sys}}, t_H]$ ; red cross), or whether the simulations are ‘converged’ ( $t_H < \text{MIN}[T_{\text{sys}}, T_{\text{dis}}]$ ; solid green square). The dashed lines correspond to Eq. (10), and indicates the typical resolution with which dark matter (sub)haloes are resolved in state-of-the-art cosmological simulations. Note that for  $r_{\text{orb}}/r_{\text{vir,h}} = 0.1$  these cosmological simulations are never converged and typically suffer from systematic errors (too much mass loss and artificial disruption). For  $r_{\text{orb}}/r_{\text{vir,h}} = 0.2$  the cosmological simulations are converged as long as  $N_p \gtrsim 10^5$ .

For those combinations of  $N_p$  and  $\varepsilon$  for which  $T_{\text{dis}} < T_{\text{sys}}$  (red crosses and green squares in left-hand panel), the middle panels of Fig. 12 plot  $T_{\text{dis}}$  as function of  $N_p$ . The grey-shaded area corresponds to time-scales longer than the Hubble time, while the blue lines are fits to the data points of the form  $T_{\text{dis}} = a_{\text{dis}}(N_p/10^5)^{1/2}$ , with the best-fit value

of  $a_{\text{dis}}$  indicated in each panel. This functional form is motivated by the notion that Poisson noise scales with  $\sqrt{N_p}$ , and provides a reasonable fit to the data, thus providing additional support for the notion that the run-away instability is driven by discreteness noise. Note that  $a_{\text{dis}}$  depends strongly on  $r_{\text{orb}}/r_{\text{vir,h}}$  and thus the strength of the tidal field; the stronger the tidal field, the stronger the amplification of the discreteness noise.

Finally, for those combinations of  $N_p$  and  $\varepsilon$  that result in a systematic overestimation of the mass loss rate (red solid dots in left-hand panels), the right-hand panels of Fig. 12 plot  $T_{\text{sys}}$  as function of  $\varepsilon$ . Clearly  $T_{\text{sys}}$  depends strongly on the softening length used, and only very weakly on  $N_p$ . The blue lines are fits of the form  $T_{\text{sys}} = a_{\text{sys}}(\varepsilon/0.05)^{\gamma_{\text{sys}}}$ , with the best-fit values of  $a_{\text{sys}}$  and  $\gamma_{\text{sys}}$  as indicated. Clearly,  $T_{\text{sys}}$  is much shorter in the presence of a stronger tidal field, albeit with a much weaker dependence on  $\varepsilon$ .

## 6 CRITERIA FOR NUMERICAL CONVERGENCE

In the previous sections, we have shown how inadequate force softening and discreteness noise can cause excessive mass loss and premature disruption of dark matter substructure in numerical  $N$ -body simulations. In this section we discuss under what conditions one may deem individual subhaloes, in large-scale, cosmological simulations of structure formation, adequately resolved. When analyzing such simulations, these criteria can be used to discard subhaloes that are affected by one or more of the numerical artefacts identified here, and whose properties are therefore unreliable.

### 6.1 Force Softening

In §5 we defined  $T_{\text{sys}}$  as the time when the *median*  $f_{\text{bound}}$ , obtained from a set of 10 simulations, deviates 0.1 dex from the converged results.  $T_{\text{sys}}$  is extremely sensitive to the force softening, and we therefore seek a relation between the Plummer softening length,  $\varepsilon$ , and properties of the subhalo in question that can be used to identify  $T_{\text{sys}}$ .

We are motivated by the work of Power et al. (2003), who introduced the concept of a *characteristic* acceleration,  $a_{\text{char}} = GM_{\text{vir}}/(\varepsilon r_{\text{vir}}) = V_{\text{vir}}^2/\varepsilon$ . In particular, they showed that NFW haloes *in isolation* are resolved down to a convergence radius where  $a(r) = GM(r)/r^2 \simeq a_{\text{char}}/2$ . At smaller radii  $a(r) > a_{\text{char}}/2$ , and the mass profile of the simulated halo is unreliable.

The acceleration profile,  $a(r)$ , of an NFW halo increases monotonically inwards, asymptoting to a maximum value of

$$a_{\text{max}} = \lim_{r \downarrow 0} \frac{GM(r)}{r^2} = \frac{c^2}{2f(c)} \frac{GM_{\text{vir}}}{r_{\text{vir}}^2} \quad (11)$$

where  $c$  is the NFW concentration parameter, and

$$f(x) = \ln(1+x) - \frac{x}{1+x}. \quad (12)$$

We suspect that a subhalo will no longer be properly resolved once its maximum acceleration,  $a_{\text{max}}$ , becomes smaller than of order the characteristic acceleration,  $a_{\text{char}}$ . Hence, we suspect that  $T_{\text{sys}}$  marks the time when the ratio  $a_{\text{char}}/a_{\text{max}}$  drops below some critical value of order unity.

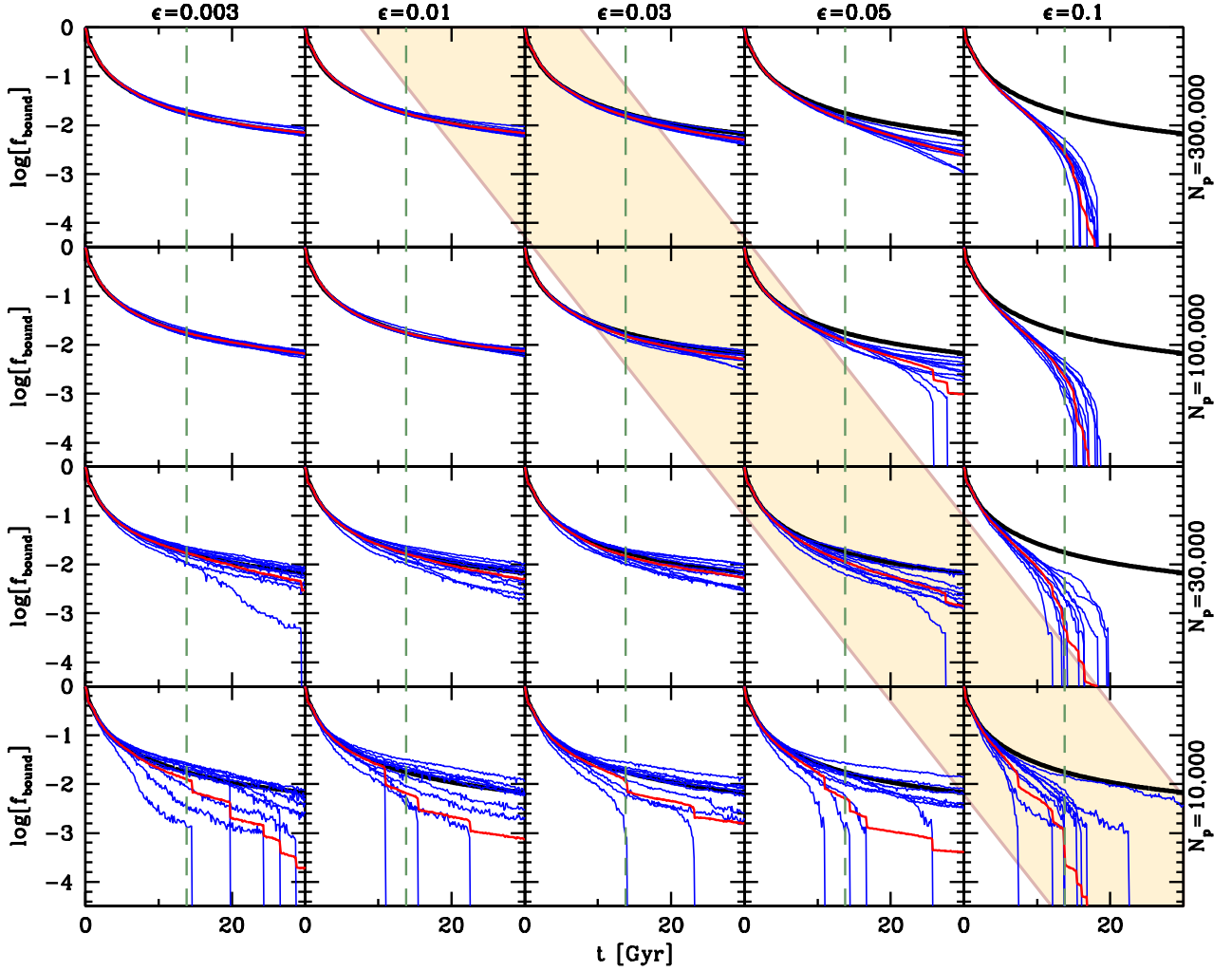


Figure 11. Same as Fig. 10, but for a circular orbit with  $r_{\text{orb}}/r_{\text{vir,h}} = 0.2$ .

In the case of a subhalo, both  $a_{\text{char}}$  and  $a_{\text{max}}$  evolve with time. Let us first focus on  $a_{\text{char}}$ . The original definition by Power et al. (2003) is based on the virial properties of the halo. Since the virial properties of a subhalo undergoing tidal mass stripping are ill-defined, we instead define the characteristic acceleration based on the subhalo's half-mass radius,  $r_h$ , according to

$$a_{\text{char}} \equiv \frac{G m_s(r_h)}{\varepsilon r_h} = \frac{G f_{\text{bound}} m_{s,0}}{2 \varepsilon r_h}. \quad (13)$$

Here  $m_{s,0}$  is the mass of the initial subhalo, i.e., prior to being introduced to the tidal field. In the case of a cosmological simulation, this roughly coincides with the mass of the subhalo at the time of accretion into the host halo. Computing  $a_{\text{max}}(t)$  for an evolving subhalo in a numerical simulation requires taking the limit of  $r$  going to zero of the enclosed mass profile. Because of the finite number of particles, computing this limit numerically is extremely noisy. Therefore instead we simply compute  $a_{\text{max}}$  for the *initial* subhalo using the analytical expression (11) for an NFW halo. Note that the central density distribution of a subhalo only undergoes relatively weak changes (cf. Fig. 2), and we therefore expect this initial  $a_{\text{max}}$  to be a reasonable representation of the maximum, central acceleration of a subhalo at any time. As we

show below, this choice is further justified by the fact that indeed  $a_{\text{char}}/a_{\text{max}}$  defined this way takes on a fixed value at  $T_{\text{sys}}$ .

Based on the above considerations, we thus expect that  $T_{\text{sys}}$  corresponds to the time when

$$\frac{a_{\text{char}}}{a_{\text{max}}} = \frac{f_{\text{bound}} f(c)}{(\varepsilon/r_{s,0})(r_h/r_{s,0})} = \chi_{\text{crit}}. \quad (14)$$

Here  $r_{s,0}$  is the scale-radius of the *initial* (i.e., at accretion) subhalo, and the value of the free parameter,  $\chi_{\text{crit}}$ , is to be determined from our numerical experiments. We do so as follows: for each combination  $(N_p, \varepsilon)$  for which the simulations discussed in §5 suffer from systematic errors (i.e.,  $T_{\text{sys}} < T_{\text{dis}}$ ), we compute  $r_h$  and  $f_{\text{bound}}$  at the time  $T_{\text{sys}}$ . The left-hand panel of Fig. 13 plots the resulting  $\log f_{\text{bound}}$  versus  $\log[\varepsilon r_h]$  (in model units, for which  $r_{s,0} = 1$ ). Errorbars on  $r_h$  and  $f_{\text{bound}}$  are obtained from the scatter in these properties among the 10 simulations at  $T_{\text{sys}}$ , and are typically smaller than the symbols. Clearly, there is an extremely tight relation between these parameters, which is independent of the subhalo's orbit and well described by

$$f_{\text{bound}} = 1.2 \left( \frac{\varepsilon}{r_{s,0}} \right) \left( \frac{r_h}{r_{s,0}} \right), \quad (15)$$

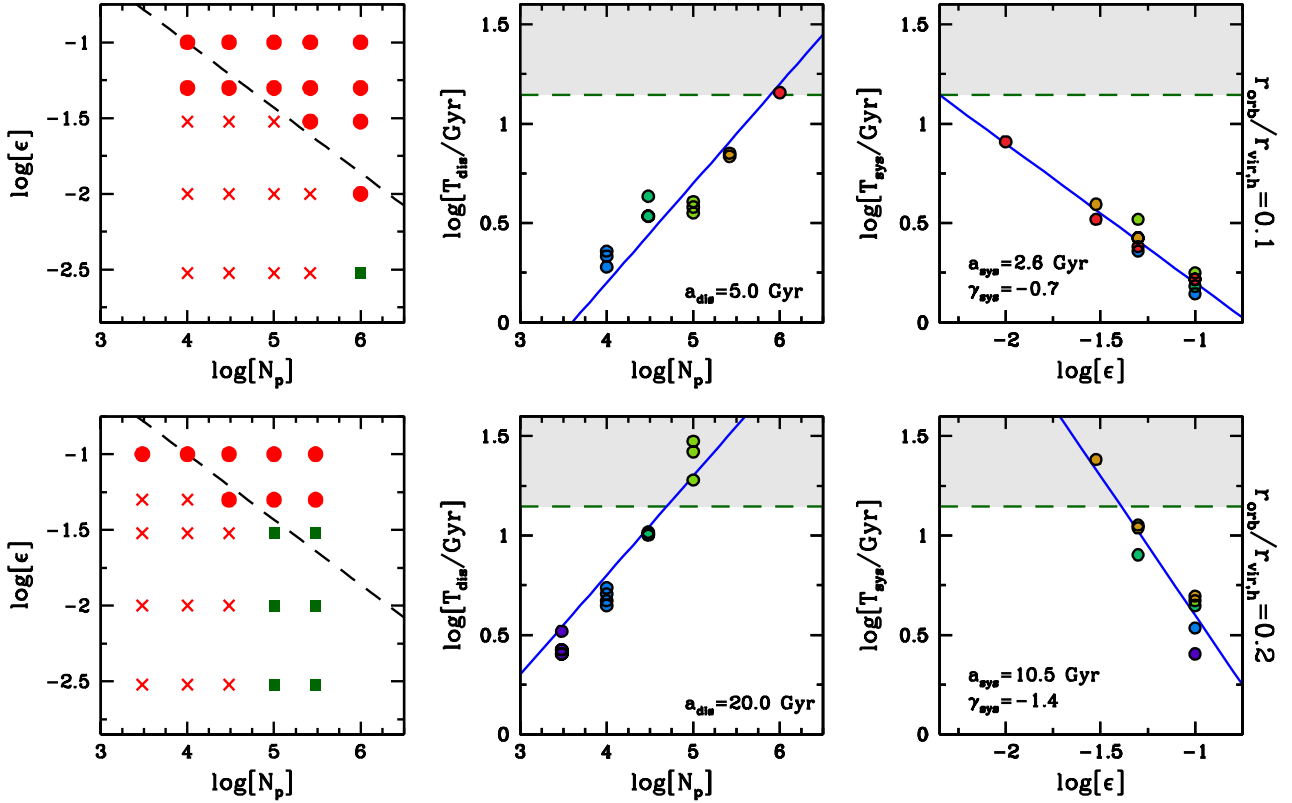


**Figure 12.** *Left-hand panels:* For each set of 10 simulations in  $(N_p, \epsilon)$ -parameter space, the symbols indicate whether the simulations suffer from discreteness noise (red crosses), from systematic errors (solid red circles), or whether the simulations are ‘converged’ (solid green square). The dashed lines indicate the typical resolution with which dark matter (sub)haloes are resolved in state-of-the-art cosmological simulations (Eq. [10]). *Middle panels:* The discreteness time,  $T_{\text{dis}}$  as function of  $N_p$ , for those simulations with  $T_{\text{dis}} < T_{\text{sys}}$ . The grey-shaded area corresponds to time-scales longer than the Hubble time, while blue lines are fits to the data of the form  $T_{\text{dis}} = a_{\text{dis}} N_p^{1/2}$ , with the best-fit value of  $a_{\text{dis}}$  indicated in each panel. *Right-hand panels:* The systematic time,  $T_{\text{sys}}$  as function  $\epsilon$  for those simulations with  $T_{\text{sys}} < T_{\text{dis}}$ . Blue lines are fits of the form  $T_{\text{sys}} = a_{\text{sys}}(\epsilon/0.05)^{\gamma_{\text{sys}}}$ , with the best-fit values of  $a_{\text{sys}}$  and  $\gamma_{\text{sys}}$  as indicated. In each column, top and bottom panels correspond to simulations with  $r_{\text{orb}}/r_{\text{vir,h}} = 0.1$  and  $0.2$ , respectively. In the middle and right-hand panels, the color of the symbols indicates  $N_p$ .

shown as the solid, red line. Substitution in Eq. (14), and using that the subhaloes in our simulation all have an initial NFW concentration parameter  $c = 10$ , we infer that  $\chi_{\text{crit}} \simeq 1.79$ . We thus conclude that dark matter subhaloes in numerical  $N$ -body simulations are only properly resolved as long as

$$f_{\text{bound}} > \frac{1.79}{f(c)} \left( \frac{\epsilon}{r_{s,0}} \right) \left( \frac{r_h}{r_{s,0}} \right) \quad (16)$$

where  $r_{s,0}$  and  $c$  are the scale radius and concentration parameter of the (NFW) subhalo *at accretion*.

We have experimented with a number of alternative criteria, including ones in which we attempt to determine the instantaneous value of  $a_{\text{max}}$  from the numerical subhaloes. However, none of these alternatives fared any better than criterion (16). The only alternative that performed almost equally well is a simple criterion based on the ratio  $r_h/\epsilon$ . Using the same set of simulations as above we find that at  $T_{\text{sys}}$ ,  $\log(r_h/\epsilon) = 0.84 \pm 0.14$ . This suggests that subhaloes are resolved as long as  $r_h/\epsilon > 6.9^{+2.6}_{-1.9}$ . As it turns out, this is simply another way of writing criterion (16). The reason is that our simulations reveal a reasonably tight relation be-

tween  $f_{\text{bound}}$  and  $r_h/r_{h,0}$  which is well approximated by

$$\frac{r_h}{r_{h,0}} \simeq 0.7 f_{\text{bound}}^{0.5} \quad (17)$$

over the range where  $-2.5 \lesssim \log(f_{\text{bound}}) \lesssim -0.5$ . Substitution in Eq. (16) and using the relation between the half-mass radius and scale-radius of an NFW halo (Eq. [8]), we can rewrite Eq. (16) as

$$\frac{r_h}{\epsilon} > 0.62 \frac{c^{1.26}}{f(c)}. \quad (18)$$

For  $c = 10$ , the value adopted for all subhaloes in our simulations, the right-hand side of this criterion is equal to 7.6, in excellent agreement with the average ratio of  $r_h/\epsilon$  inferred from our simulations at  $T_{\text{sys}}$ . Since relation (17) reveals a fair amount of variance among simulations, especially for small values of  $f_{\text{bound}}$ , we generally recommend using criterion (16) over criterion (18).

## 6.2 Discreteness Noise

We now derive a criterion that can be used to check whether a subhalo in a numerical  $N$ -body simulation is significantly



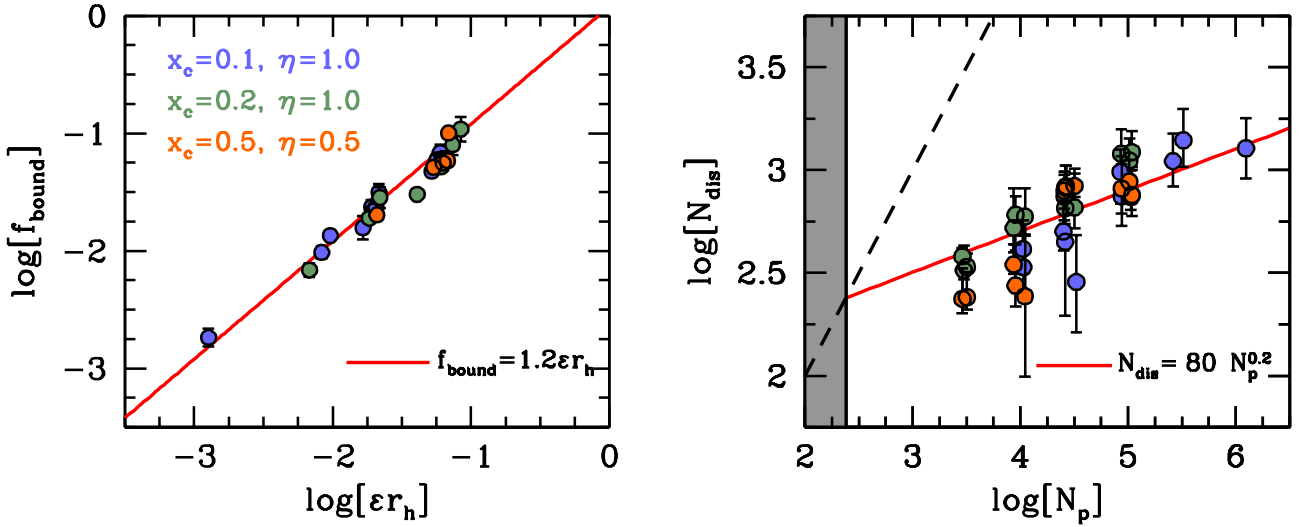


**Figure 13.** *Left-hand panel:* The bound fraction at  $T_{\text{sys}}$  as a function of the product of the half-mass radius at that time,  $r_h$ , and the softening length,  $\epsilon$ . As is evident, these parameters are tightly correlated, indicating that  $N$ -body simulations fail to resolve the tidal evolution of subhaloes once they violate the conditions specified by criterion (16). *Right-hand panel:* The average number of bound particles,  $N_{\text{dis}}$ , in a subhalo at time  $T_{\text{dis}}$ , when discreteness noise triggers a runaway instability. Results are plotted as function of  $N_p$ , the number of particles in the initial subhalo. Errorbars indicate the 68 percent confidence intervals, and the solid, red line corresponds to the best-fit relation following the scaling expected for Poisson noise (see Appendix A). The dashed line corresponds to  $N_{\text{dis}} = N_p$ , while the gray-shaded region indicates where  $N_p < 240$ . Such subhaloes are adversely affected by discreteness noise from the moment they are accreted by their hosts. In both panels blue and green symbols correspond to simulations of circular orbits with  $r_{\text{orb}}/r_{\text{vir,h}} = 0.1$  and  $0.2$ , respectively, while the orange symbols correspond to an eccentric orbit with  $x_c = \eta = 0.5$ .

affected by discreteness noise. Since this is purely a manifestation of finite particle number, we seek a criterion that depends on the number of particles that is used to model the subhalo. In §5 we defined the characteristic time  $T_{\text{dis}}$  as the time when the standard deviation in  $f_{\text{bound}}$  among 10 simulations becomes 0.1 dex. We now define  $N_{\text{dis}}$  as the average number of particles in the subhalo remnant at this time  $T_{\text{dis}}$ .

We compute  $N_{\text{dis}}$  for each combination of  $(N_p, \epsilon)$  for which the simulations suffer from discreteness noise (i.e.,  $T_{\text{dis}} < T_{\text{sys}}$ ). Since  $\sigma_{\log f}$  is estimated from only 10 simulations, it carries an error, which in turn imposes an error on  $N_{\text{dis}}$ . To estimate this error we proceed as follows. Under the assumption that  $\log f_{\text{bound}}$  at any given epoch follows a log-normal distribution, the fractional error on the standard deviation estimated from  $N$  realizations of that distribution is equal to  $1/\sqrt{2(N-1)}$  (e.g., Taylor 1997). Hence, for  $N = 10$  we have that the fractional error on  $\sigma_{\log f}$  is 0.236. We then estimate the upper and lower bounds of the 68 percent confidence interval on  $N_{\text{dis}}$  as the values for  $\langle N_{\text{dis}} \rangle$  at the times when  $\sigma_{\log f} = 0.076$  and  $\sigma_{\log f} = 0.124$ , respectively.

The results are shown in the right-hand panel of Fig. 13, which plots  $N_{\text{dis}}$  (with errorbars indicating the 68 percent confidence intervals) as a function of  $N_p$ , the number of particles in the *initial* subhalo. Typically  $300 \lesssim N_{\text{dis}} \lesssim 1000$ , with a weak trend of increasing  $N_{\text{dis}}$  with increasing  $N_p$ . As discussed in Appendix A, because of Poisson noise in the mass loss rate of  $N$ -body subhaloes, one expects that  $N_{\text{dis}} \propto N_p^{0.2}$ . Fitting such a relation to the data, we obtain  $N_{\text{dis}} = 80 N_p^{0.2}$ , which is indicated by the red line.

Hence, in a cosmological simulation one can guard against subhaloes that are potentially affected by discreteness

noise by only selecting subhaloes that obey the following criterion:

$$N > 80 N_{\text{acc}}^{0.2}. \quad (19)$$

Here  $N_{\text{acc}}$  is the number of particles in the subhalo at its moment of accretion. Note that subhaloes with  $N_{\text{acc}} < 80^{5/4} \simeq 240$  always violate this criterion, and therefore are susceptible to discreteness noise immediately after accretion. In other words,  $N$ -body simulations are unable to properly resolve the tidal evolution of dark matter subhaloes with  $N \lesssim 250$  particles at accretion.

### 6.3 Eccentric Orbits

Thus far we have focused exclusively on circular orbits. In reality, though, subhaloes move on eccentric orbits with fairly large apo-to-pericentre ratios (e.g. Tormen 1997; Ghigna et al. 1998; van den Bosch et al. 1999). As a consequence, they are significantly impacted by impulsive heating due to tidal shocks at pericentric passage (see Paper I), something that is not accounted for in our simulations of circular orbits. This begs the question to what extent the criteria derived above are applicable to the more realistic, eccentric orbits. In order to address this, we have performed a set of simulations, similar to those used above, but for an eccentric orbit with  $x_c \equiv r_c(E)/r_{\text{vir}} = 0.5$  and an orbital circularity of  $\eta \equiv L/L_c(E) = 0.5$ . Here  $E$  and  $L$  are the orbital energy and angular momentum, respectively,  $r_c(E)$  is the radius of a circular orbit of energy  $E$ , and  $L_c(E)$  is the corresponding angular momentum. Note that a circularity of  $\eta = 0.5$  is characteristic of orbits at infall (e.g. Zentner et al. 2005; Wetzel 2011; Jiang et al. 2015; van den Bosch 2017),

We adopt the fiducial parameters for the masses and

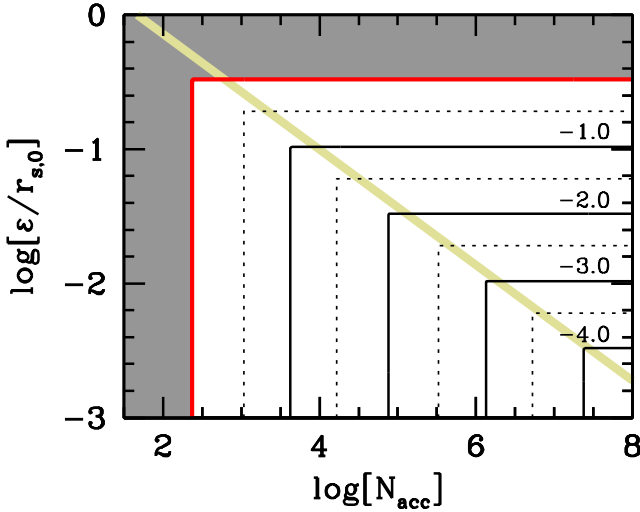


**Figure 14.** Contour plot of the minimal bound mass fraction,  $f_{\text{bound}}^{\text{min}}$ , defined by Eq.(22), in the parameter space of  $N_{\text{acc}}$ , the number of particles of the subhalo at accretion, and  $\varepsilon/r_{s,0}$ , the softening length in units of the subhalo's scale radius at accretion. Subhaloes with an instantaneous  $f_{\text{bound}} < f_{\text{bound}}^{\text{min}}$  are no longer reliable, and should be discarded from any analysis. Contours correspond to  $\log f_{\text{bound}}^{\text{min}} = (-4, -3.5, -3, \dots, 0)$ , with solid contours corresponding to integer values, as indicated. For comparison, the yellow-shaded band corresponds to Eq. (10), and indicates the softening length with which subhaloes of given  $N_{\text{acc}} = N_{200}$  are resolved in the Millennium simulation.

concentrations of the host and subhalo (see Table 1), and run sets of ten simulations each for different  $N_p$  and  $\varepsilon$ . For each of these sets, we determine  $T_{\text{sys}}$  and  $T_{\text{dis}}$  as described in §5.1, and we test whether these simulations are subject to the same criteria as the circular orbits discussed above. The results, based on a sample of 200 simulations with  $3000 \leq N_p \leq 100,000$  and  $0.003 \leq \varepsilon \leq 0.1$  are shown as the orange symbols in Fig. 13. Note how the results for the eccentric orbit are in excellent agreement with the relations for the circular orbits. This strongly suggests that criteria (16) and (19) are valid for orbits of all energies and angular momenta (see §8).

#### 6.4 The Minimal Bound Mass Fraction

Both criteria (16) and (19) can be cast in a constraint on the bound mass fraction,  $f_{\text{bound}}$ , for a given set of numerical parameters  $(N_p, \varepsilon)$ . For criterion (16) this is achieved by using Eqs. (17) and (8), which yields

$$f_{\text{bound}} > f_{\text{bound}}^{\text{min},1} = 1.12 \frac{c^{1.26}}{f^2(c)} \left( \frac{\varepsilon}{r_{s,0}} \right)^2. \quad (20)$$

For criterion (19) one simply divides both sides by  $N_{\text{acc}}$  to obtain

$$f_{\text{bound}} > f_{\text{bound}}^{\text{min},2} = 0.32 \left( \frac{N_{\text{acc}}}{1000} \right)^{-0.8}. \quad (21)$$

We now define

$$f_{\text{bound}}^{\text{min}} \equiv \text{MAX}[f_{\text{bound}}^{\text{min},1}, f_{\text{bound}}^{\text{min},2}] \quad (22)$$

such that subhaloes with an instantaneous bound mass fraction  $f_{\text{bound}} > f_{\text{bound}}^{\text{min}}$  may be deemed converged, while those

subhaloes for which  $f_{\text{bound}}$  is smaller than this minimal value are unreliable; either because of discreteness noise, or because of inadequate force softening.

Fig. 14 shows contours of  $f_{\text{bound}}^{\text{min}}$  in the  $(N_{\text{acc}}, \varepsilon)$  parameter space. This figure can be used to read off whether a particular subhalo in a cosmological simulation may be deemed converged or not. Note that the dark-grey shaded region indicates the part of parameter space for which  $f_{\text{bound}}^{\text{min}} > 1$ ; subhaloes with these parameters can never be deemed converged (i.e.,  $N_{\text{acc}} \lesssim 250$  or  $\varepsilon \gtrsim 0.3r_{s,0}$ ). For comparison, the yellow-shaded band corresponds to Eq. (10), and indicates the softening length with which subhaloes of given  $N_{\text{acc}} = N_{200}$  are resolved in the Millennium simulation. It shows that subhaloes in this simulation with  $f_{\text{bound}} < 0.01$  ( $< 0.001$ ) can only be deemed converged if  $N_{\text{acc}} \gtrsim 10^5$  ( $> 10^6$ ).

Finally, we emphasize that although the results in Fig. 14 depend on the concentration parameter of the subhalo at accretion (here we have adopted  $c = 10$ ), this dependence is very weak: for  $5 < c < 30$  (the typical range of concentration parameters for CDM haloes), the factor  $c^{1.26}/f^2(c)$  only ranges between 8 and 12, and therefore has almost negligible impact on the value of  $f_{\text{bound}}^{\text{min}}$ .

## 7 SENSITIVITY TO INITIAL CONDITIONS

In §4 we discussed how the numerical parameters  $\Delta t$ ,  $\theta$ ,  $\varepsilon$  and  $N_p$ , impact the outcome of numerical  $N$ -body simulations of the tidal evolution of dark matter substructure. In addition to setting these numerical parameters, the simulator also needs to decide on how to pick and set the initial conditions (ICs) for the simulation. As already eluded to in §2.1, this is non-trivial. In this section we therefore examine how the simulation outcome depends on subtle issues related to setting the ICs. We start with the actual method that is used to pick the phase-space coordinates of the particles that make up the subhalo. Next we discuss the impact of letting the subhalo relax prior to placing it in the external tidal field of the host halo, and the impact of truncating the subhalo at its tidal radius.

All simulations presented below use the fiducial physical and numerical parameters of Table 1. In addition, for comparison we also run each of these simulations with a five times smaller softening length,  $\varepsilon = 0.01$ .

### 7.1 Local Maxwellian Approximation

In all simulations discussed thus far we have set-up the initial conditions for the NFW halo by sampling the isotropic distribution function,  $f(E)$ , as described in §2.1. An alternative method, which has been applied in numerous studies (e.g., Hernquist 1993; Springel & White 1999; Klypin et al. 1999a; Mayer et al. 2001; Peñarrubia et al. 2002; Taffoni et al. 2003; Hayashi et al. 2003), is to use the local Maxwellian approximation (hereafter LMA), which is based on the ansatz that the velocity distribution at any given position can be approximated by a multivariate Gaussian, whose velocity dispersion follows from solving the Jeans equation at that position. In detail, one proceeds as follows. One first draws a radius,  $r$ , using the enclosed mass profile of the halo in question, followed by two angles that

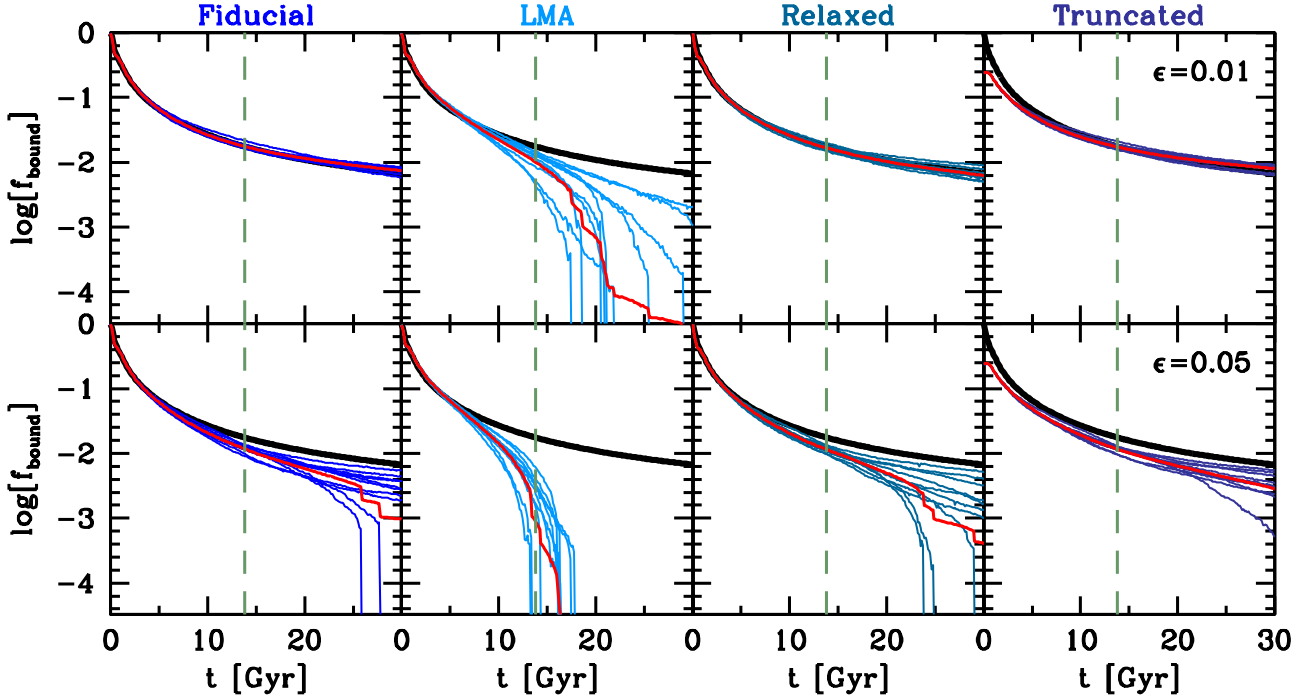


**Figure 15.** Blue lines show the bound mass fractions as function of time for sets of 10 simulations with  $N_p = 10^5$  each, of subhaloes on a circular orbit with  $r_{\text{orb}}/r_{\text{vir,h}} = 0.2$  in a host halo with  $M_h = 1000m_{s,0}$  and  $c_h = 5.0$ . The red line shows the corresponding average, while the solid, black line shows converged results from a simulation with  $N_p = 10^7$  and  $\epsilon = 0.003$ . Top and bottom panels correspond to simulations run with a force softening length of  $\epsilon = 0.01$  and  $0.05$ , respectively. Different columns correspond to different methods used to initialize the subhaloes. The columns labeled ‘Fiducial’ and ‘LMA’ shows results in which the initial positions and velocities are drawn from the distribution function,  $f(E)$ , and based on the local Maxwellian approximation, respectively. In the case of the columns labeled ‘Relaxed’ and ‘Truncated’ the initial subhaloes were allowed to relax for 10 Gyr and truncated at the tidal radius, respectively, prior to being placed in the tidal field of the host halo. See text for details.

allow one to assign the particle Cartesian coordinates. Next, one computes the local, radial velocity dispersion,  $\sigma_r^2(r)$ , by solving the Jeans equation (for an NFW halo, the solution is given by Eq. 11 in van den Bosch et al. 2004). Assuming isotropy, one then obtains the local Cartesian velocities by drawing three Gaussian deviates with a dispersion equal to  $\sigma_r(r)$ . We follow Hernquist (1993), and redraw the Cartesian velocity components if the resulting 3D speed exceeds 95 percent of the local escape speed. The advantage of this method over our fiducial one is that it is easier to implement and avoids having to compute and sample the DF (see discussion in Hernquist 1993). However, the method is only approximate, in that it ignores higher order moments of the collisionless Boltzmann equation, and it has been demonstrated that the local Maxwellian approximation can yield ICs that are far from equilibrium; as a consequence, N-body realizations of such models rapidly relax to a steady-state that can differ significantly from the initial, intended one (Kazantzidis et al. 2004b).

Most importantly, Kazantzidis et al. (2004b) compared the tidal evolution of two subhaloes on the same orbit; one whose ICs were obtained using the LMA, and the other for which the phase-space coordinates are drawn self-consistently from the (isotropic) distribution function,  $f(E)$ . They find that the subhalo constructed under the assumption that the local velocity field is Maxwellian is completely disrupted in a few orbits, whereas the self-consistent subhalo survives for the entire duration of the simulation.

Kazantzidis et al. (2004b) therefore conclude that the LMA method for generating ICs results in a systematic bias regarding the tidal evolution of substructure. However, there is an important caveat here, in that they simulated each of their subhaloes with only  $N_p = 10^5$  particles. As demonstrated in this paper, such simulations are subject to severe discreteness noise. Hence, the difference in  $f_{\text{bound}}(t)$  for the two subhaloes might simply reflect discreteness noise, i.e., the LMA-initialized subhalo, *by chance*, happened to undergo disruption due to the discreteness-driven run-away instability, rather than due to a *systematic* difference arising from the different methods used to draw the initial phase-space coordinates.

To test this, we construct two *ensembles* of 10 subhaloes with  $N_p = 10^5$  each. The first is our ‘fiducial’ ensemble, in which the initial positions and velocities of the particles are drawn from the DF,  $f(E)$ , using our fiducial method outlined in §2.1. Ensemble members only differ in their random realizations. The second ensemble consists of random realizations based on the LMA method described above. Note that both methods assume that the distribution function is isotropic. For each of these 20 subhaloes we run two simulations; one with  $\epsilon = 0.01$  and the other with  $\epsilon = 0.05$ . In each case the subhalo is placed on a circular orbit with  $r_{\text{orb}}/r_{\text{vir,h}} = 0.2$  in a host halo with  $M_h = 1000m_{s,0}$  and  $c_h = 5.0$ , and evolved for 30 Gyr.

The results are shown in Fig. 15 where the first and second columns from the left show the results for the fiducial

and LMA ensembles, respectively. There is a clear difference, in that the LMA-based subhaloes experience *systematically* more mass loss, almost always resulting in premature disruption. This ratifies the conclusion by Kazantzidis et al. (2004b), that the local Maxwellian approximation for setting up the initial conditions of subhaloes, results in accelerated mass loss, leading to their artificial disruption. As discussed in Kazantzidis et al. (2004b), the reason for this systematic difference is that subhaloes initialized using the LMA method are far from equilibrium, and quickly relax to a state with a much shallower central density distribution.

## 7.2 Initial Relaxation

As discussed in §2.1, the initial haloes in our fiducial ensemble are not in perfect equilibrium. First of all, we instantaneously truncate the halo at its own virial radius, without accounting for this truncation in  $f(E)$ . Secondly, we do not account for the simulation's force softening when setting up the initial conditions. And thirdly, by placing the initial halo in a tidal field, we instantaneously introduce tidal perturbations that are not accounted for in the ICs.

To gauge the impact of these shortcomings, we perform two different tests. First, we perform a set of simulations in which we first evolve the subhaloes in our fiducial ensemble for 10 Gyr in isolation, prior to placing them in the tidal field of their host haloes (using the same  $r_{\text{orb}}/r_{\text{vir,h}} = 0.2$  orbit as above). This allows the subhalo to relax, and to reach virial equilibrium, before being introduced to its external, tidal field. The results, again for  $\varepsilon = 0.01$  and  $0.05$ , are shown in the third column of Fig. 15. Note that these are virtually indistinguishable from our fiducial simulations (left-most column), indicating that our simulation results are not influenced by the fact that their initial conditions are not in perfect equilibrium.

## 7.3 Initial Tidal Truncation

As a second test, we truncate the initial subhalo at its tidal radius, which for a circular orbit at radius  $r_{\text{orb}}$  is given by

$$r_t = r_{\text{orb}} \left[ \frac{m_{s,0}(r_t)/M_h(r_{\text{orb}})}{3 - \frac{d \ln M_h}{d \ln r}|_{r_{\text{orb}}}} \right]^{1/3}, \quad (23)$$

(see Paper I for details). One might argue that such an initial truncation is more realistic, as the subhalo is expected to have already experienced tidal stripping on its way to the initial position in the host halo. And if stripping were to simply remove all particles beyond its tidal radius, this ‘tidal truncation’ seems appropriate. Indeed, some studies have used a similar ‘pre-truncation’ in their simulations (e.g., Choi et al. 2007).

To test the impact of this ‘initial truncation’ we proceed as follows. For each subhalo in our fiducial ensemble, which has  $N_p = 10^5$  and is initially truncated at its virial radius, we remove all particles with  $r > r_t$ . In the case of  $r_{\text{orb}}/r_{\text{vir,h}} = 0.2$  and our fiducial halo concentrations (see Table 1),  $r_t = 0.183r_{\text{vir,s}}$ , which encloses on average about 26.5 percent of the subhalo’s virial mass. Hence, the average number of particles with which this new ensemble of ‘tidally truncated’ subhaloes is resolved is  $N_p = 26,500$ . The results

of integrating each of these subhaloes for 30 Gyr along a circular orbit with  $r_{\text{orb}}/r_{\text{vir,h}} = 0.2$  are shown in the right-most column of Fig. 15. Once again, the results are very similar to those of our fiducial ensemble, although some differences are apparent for the simulations with  $\varepsilon = 0.05$ . These arise from differences in the amount of dynamical self-friction, which is suppressed in the tidally truncated ensemble compared to the fiducial ensemble. The reason is that there is far more tidally stripped material in the latter, resulting in a larger reduction of the orbital radius. However, the effect is extremely small, and does not have a significant impact on any of the simulation results presented here.

To summarize, we confirm the conclusion of Kazantzidis et al. (2004b) that using the local Maxwellian approximation to initialize subhaloes results in excessive mass loss and premature, artificial disruption. Although the ICs of our subhaloes are not in perfect equilibrium, we have shown that this has no discernible impact on the final outcome of our simulations. Also, the fact that the subhalo is instantaneously introduced into the external tidal field of the host halo, does not have a significant impact, in that pre-truncating the subhalo at its tidal radius yields very similar results. We thus conclude that the simulation results presented in this paper are meaningful and relevant despite the non-physical nature of the ICs.

## 8 POTENTIAL CAVEATS

The results presented here and in Paper I suggest that most, if not all, subhalo disruption in numerical simulation is numerical, and cast some serious doubt on the belief that the subhalo mass functions in cosmological numerical simulations are properly converged (i.e., are reliable) down to a mass limit of 50-100 particles. However, before we can claim that existing simulations are significantly in error, we have to address a number of caveats:

- **Parameter Space:** One of the main limitations of this study is that we have only covered a tiny fraction of parameter space. In particular, we focused (almost) exclusively on circular orbits, while keeping the masses and concentration parameters of the host and subhalo fixed to the fiducial values listed in Table 1. In reality subhalo orbits span a wide range of energies and angular momenta. Typically, along more eccentric orbits the subhaloes experience more impulsive heating due to tidal shocks at pericentric passage<sup>5</sup>, something that is absent along the circular orbits examined here. The tidal evolution of a subhalo also strongly depends on the concentrations of both the subhalo and the host halo, while the mass ratio of the host and sub-halo mainly controls the strength of dynamical friction (and self-friction). We emphasize, though, that our results assess the impact of numerics relative to high-resolution, converged simulations. Since we do not expect this *relative* behavior to be strongly affected by these physical parameters, we conjecture that our results remain valid for most of the relevant

<sup>5</sup> As shown in Paper I, the impulsive heating due to encounters with other subhaloes, sometimes called ‘harassment’ is negligible in comparison.



parameter space. Although our test based on a single eccentric orbit (§6.3) clearly supports this conjecture, ideally this should be repeated for other orbital configurations, mass ratios and/or halo concentration parameters. However, given the limiting amount of resources and man-power available, and given that the study presented here is already based on many hundreds of simulations, such an extension is beyond the scope of the research presented here.

- **Host Halo Realism:** One aspect of our simulations that may potentially impact some of the outcome is the fact that we treated the host halo as a spherical, static and analytical potential. In reality, haloes are non-spherical, dynamical objects, typically growing in mass, undergoing mergers and violent relaxation. This impacts the orbits and hence the amount of tidal stripping and heating. In addition, in a ‘live’ host halo (i.e., modeled as an  $N$ -body system, rather than an analytical potential), the subhalo will experience dynamical friction, in addition to the self-friction briefly discussed in §3.2. Although such dynamical friction is not significant for the mass ratio considered here ( $M_h/m_{s,0} = 1000$ ), it will play an important role for systems where  $M_h/m_{s,0} \lesssim 30$  (e.g., Mo et al. 2010). Unfortunately, the only way to take proper account of all these effect is by simulating the system in its proper cosmological setting, and thus to run a cosmological simulation. However, doing so with the resolution required to achieve proper convergence, as specified here, is beyond the capabilities of present-day technology.

- **Impact of baryons:** Finally, we emphasize that this work has focused exclusively on dark matter only, without taking account of potential baryonic effects. There is a rapidly expanding literature on how baryons may impact the abundance and demographics of dark matter substructure (e.g., Macciò et al. 2006; Weinberg et al. 2008; Dolag et al. 2009; Arraki et al. 2014; Brooks & Zolotov 2014; Despali & Vegetti 2016; Fiacconi et al. 2016; Wetzel et al. 2016; Garrison-Kimmel et al. 2017). Our work, in no way, aims to undermine the importance of baryons. However, before we can make reliable predictions for how baryonic processes modify substructure in the dark sector, we first need to establish a better understanding of how tides impact substructure, and develop tools and criteria to assess the reliability of simulations (be it hydro or  $N$ -body). Hence, this work is to be considered a necessary first step towards a more reliable treatment of dark matter substructure (including satellite galaxies); not the final answer.

## 9 CONCLUSIONS & DISCUSSION

As part of our ongoing effort to understand the origin of the ubiquitous disruption of dark matter subhaloes in numerical simulations (see van den Bosch 2017), we have performed a large suite of hundreds of idealized simulations that follow the tidal evolution of individual  $N$ -body subhaloes in a fixed, analytical host halo potential. The goal of these idealized, numerical experiments is not to simulate realistic astrophysical systems, but rather to gain a physical understanding of the complicated, non-linear and numerical processes associated with the tidal stripping of dark matter subhaloes. This is facilitated by restricting ourselves to purely circular orbits

(i.e., no tidal shock heating), and by focusing exclusively on dark matter (i.e., no baryons).

By varying the orbital radius (strength of the tidal field), the number of particles (mass resolution), the force softening (force resolution), the tree opening angle (force accuracy) and the time step used (time resolution), we address the following specific questions: (i) is the disruption artificial (numerical) or real (physical), (ii) under what conditions do subhaloes disrupt, and what causes it, and (iii) what are the numerical requirements to properly resolve the tidal evolution of dark matter substructure?

We confirm the conclusions from our mainly analytical assessment in Paper I that most, if not all, disruption of substructure in  $N$ -body simulations is numerical in origin (see also Kazantzidis et al. 2004a; Goerdt et al. 2007; Diemand et al. 2007b,a; Peñarrubia et al. 2010, all of whom have argued that complete disruption of CDM subhaloes is extremely rare). As long as a subhalo is resolved with sufficient mass and force resolution, a bound remnant survives, even if the subhalo has lost more than 99.9 percent of its original (infall) mass. We thus conclude that state-of-the-art cosmological simulations still suffer from significant overmerging. We have demonstrated that this is mainly due to inadequate force-softening. In addition, we have shown that subhaloes in  $N$ -body simulations are susceptible to a runaway instability which is triggered by the amplification of discreteness noise in the presence of a tidal field. These two processes conspire to put some serious limitations on the reliability of dark matter substructure in state-of-the-art cosmological simulations. In addition, in cosmological simulations discreteness effects also inject artificial structure during the collapse of sheets and filaments (e.g., Weinberg 1993; Angulo et al. 2013; Power et al. 2016), which further muddles the waters.

We have used our large suite of simulations to gauge under what conditions inadequate force softening and discreteness noise impact subhaloes. We find that properly resolving the tidal evolution of a subhalo on a circular orbit at 10 percent of the host halo’s virial radius, requires that the subhalo is simulated with at least  $N_p = 10^6$  particles and with a softening length,  $\varepsilon$ , that is only  $\sim 0.003$  times the subhalo’s (NFW) scale radius,  $r_s$ . These requirements, though, depend strongly on the strength of the tidal field. For example, on a circular orbit at 20 percent of the host halo’s virial radius,  $N_p = 10^5$  and  $\varepsilon/r_s = 0.03$  suffice to properly resolve its tidal evolution for at least a Hubble time. More generally, we find that subhaloes in numerical simulations start to be significantly affected by discreteness noise once

$$f_{\text{bound}} < 0.32(N_{\text{acc}}/1000)^{-0.8}, \quad (24)$$

where  $N_{\text{acc}}$  is the number of particles in the subhalo at accretion. Similarly, subhaloes in numerical simulations are systematically affected by inadequate force resolution (often leading to artificial disruption), once

$$f_{\text{bound}} < \frac{1.79}{f(c)} \left( \frac{\varepsilon}{r_{s,0}} \right) \left( \frac{r_h}{r_{s,0}} \right), \quad (25)$$

where  $c$  is the NFW concentration parameter of the subhalo at accretion, and  $r_h$  is the instantaneous half-mass radius. These two criteria can be used to assess whether individual subhaloes in cosmological simulations are reliable or not.

In fact, we recommend that subhaloes that satisfy either of these two criteria be discarded from further analysis.

As discussed at length in Paper I, being able to accurately predict the abundance and demographics of dark matter substructure is of crucial importance for a wide range of astrophysics. First of all, it is one of the prime discriminators between different dark matter models; if dark matter is warm (WDM), rather than cold, free-streaming and enhanced tidal disruption, will cause a significantly reduced abundance of *low mass* subhaloes (e.g., Knebe et al. 2008; Lovell et al. 2014; Colín et al. 2015; Bose et al. 2016). If dark matter has a significant cross-section for self-interaction (SIDM), subhaloes are predicted to have constant-density cores, with significantly lower central densities than their cold dark matter (CDM) counterparts (e.g. Vogelsberger et al. 2012; Rocha et al. 2013). Dark matter substructure also boosts the expected dark matter annihilation signal (Bergström et al. 1999), an effect that is typically quantified in terms of a ‘boost-factor’ (e.g., Strigari et al. 2007; Giocoli et al. 2008b; Kuhlen et al. 2008; Pieri et al. 2008; Moliné et al. 2016). In addition, dark matter substructure is also important for understanding galaxy formation and large scale structure. Dark matter subhaloes are believed to host satellite galaxies and their demographics is therefore directly related to the (small scale) clustering of galaxies. This idea underlies the popular technique of subhalo abundance matching (e.g., Vale & Ostriker 2004; Conroy et al. 2006; Guo et al. 2010; Hearin et al. 2013; Moster et al. 2013; Behroozi et al. 2013), which has become a prime tool for interpreting galaxy clustering, galaxy-galaxy lensing, and group multiplicity functions, and is even used to constrain cosmological parameters (Marín et al. 2008; Trujillo-Gomez et al. 2011; Hearin et al. 2015, 2016; Reddick et al. 2013, 2014; Zentner et al. 2014, 2016; Lehmann et al. 2015).

The results presented here instill some serious concern regarding the reliability of dark matter substructure in state-of-the-art cosmological simulations. In particular, it questions whether the fact that subhalo mass functions appear to be converged down to 50-100 particles per subhalo (see §1) implies that the results are reliable. For example, as shown in Fig. 10, even subhaloes with as many as  $10^6$  particles at accretion can experience artificial disruption and/or discreteness noise. On the other hand, although our results make it clear that the properties (e.g., mass, size, maximum circular velocity, concentration) of *individual* subhaloes can no longer be trusted once they violate criterion (19), it remains to be seen to what extent these results impact *statistical* results, such as the subhalo mass function. For example, subhaloes that violate criterion (19) have mass loss rates that are severely affected by a discreteness noise driven runaway instability. In  $\sim 50$  percent of the cases this results in the subhaloes losing too much mass, while the other half experience mass loss rates that are too low. As a consequence, discreteness noise does not strongly affect the *average* mass loss rate, and it remains to be seen whether its overall effect on the subhalo mass (or velocity) function is significant. We intend to address this issue in the near future (Ogiya et al., in preparation) using a series of idealized, high-resolution, converged simulations (similar to the converged simulations used here to gauge the impact of numerics), that span a wide range of parameter space (orbital energy and

circularity, as well as the concentration parameters of the host and sub-halo). Such a data-base can be used to calibrate semi-analytical models describing the build-up and evolution of dark matter substructure (e.g., Taylor & Babul 2001; Peñarrubia & Benson 2005; van den Bosch et al. 2005; Zentner et al. 2005; Jiang & van den Bosch 2016b), which in turn can be used to correct cosmological simulations for artificial subhalo disruption. This data-base will also be instrumental for informing and facilitating a more accurate modeling of ‘orphan galaxies’ in semi-analytical models of galaxy formation (e.g., Springel et al. 2001; Kang et al. 2005; Kitzbichler & White 2008), subhalo abundance matching models (e.g., Conroy et al. 2006; Guo & White 2013; Campbell et al. 2017) and empirical models (e.g., Moster et al. 2010, 2017; Lu et al. 2014). We refer the reader to Tollet et al. (2017) and Pujol et al. (2017) for detailed discussions regarding the various methods that are being used to treat such orphans.

We end with a brief discussion of how to proceed. In particular, how can we improve numerical simulations such that overmerging is less of an issue? The only way to overcome the discreteness driven runaway instability is to increase the mass resolution (i.e., increase the number of particles used in the simulations). As computer power continues to increase, so will the mass resolution of the state-of-the-art cosmological simulations. Consequently, at a fixed mass, the resolution will undoubtedly continue to improve, thereby suppressing issues related to discreteness noise. However, criterion (24) will remain valid, and there will thus always be a mass scale below which subhaloes are no longer treated reliably. Overcoming the *systematic* issue of inadequate force softening is far more challenging. Ideally, the softening scale varies with both space and time. Few studies have attempted to implement such adaptive softening strategies in particle-based  $N$ -body codes. Price & Monaghan (2007) and Iannuzzi & Dolag (2011) implemented schemes in which the softening adapts to the local density (softening scale decreases with increasing density), while retaining conservation of both momentum and energy. Hobbs et al. (2016) even account for the anisotropy of the local density field, in an attempt to overcome the problem of artificial fragmentation that plagues simulations of structure formation in warm dark matter cosmologies. It is unclear, though, whether any of these schemes will resolve the subhalo overmerging problem. As we have shown in §4.3, the optimal softening length rapidly declines once the subhalo starts to experience mass loss, and ideally subhaloes are therefore simulated with a softening length that is significantly *smaller* than that for host haloes of a similar mass. However, due to tidal shock heating and re-virialization, the central densities of subhaloes are typically smaller than those of their host haloes (see Fig. 2). In the adaptive softening schemes mentioned above, the central regions of subhaloes would therefore be resolved with a *larger* softening length than the central region of a host halo. Until a solution to overcome numerical overmerging is found, the only option is to supplement the simulation results with a semi-analytical model. In particular, using the criteria presented in this paper one first identifies subhaloes the moment they become unreliable. Their subsequent evolution is then treated using a semi-analytical model that uses orbit integration, and treatments of tidal stripping, tidal heating and dynamical friction, to predict

their mass and location. Unfortunately, as discussed at great length in Paper I, we lack a rigorous, analytical treatment for how the mass, structure, and orbits of subhaloes evolve in the presence of a tidal field. These semi-analytical models, therefore, need to be calibrated using high-resolution, properly converged simulation results. We intend to address this ‘catch-22’ in the near future using the large data-base of idealized simulations discussed above.

## ACKNOWLEDGMENTS

This work has benefited greatly from discussions with the following individuals: Andy Burkert, Benedikt Diemer, Oliver Hahn, Andrew Hearin, Fangzhou Jiang, Johannes Lange, and Fred Rasio. We also acknowledge the referee, Chris Power, for an insightful, constructive referee report. FvdB is grateful to the Munich Excellence Cluster for its hospitality, and is supported by the Klaus Tschira Foundation and by the US National Science Foundation through grant AST 1516962. Part of this work was performed at the Aspen Center for Physics, which is supported by the National Science Foundation under grant PHY-1066293, and at the Kavli Institute for Theoretical Physics, which is supported by the National Science Foundation under grant PHY-1125915. GO is supported by funding from the European Research Council (ERC) under the European Union’s Horizon 2020 research and innovation programme (grant agreement No. 679145, project ‘COSMO-SIMS’). Some of the numerical computations were carried out on HA-PACS at the Center for Computational Sciences at University of Tsukuba.

## REFERENCES

- Angulo R. E., Hahn O., Abel T., 2013, *MNRAS*, **434**, 1756
- Arraki K. S., Klypin A., More S., Trujillo-Gomez S., 2014, *MNRAS*, **438**, 1466
- Athanassoula E., Fady E., Lambert J. C., Bosma A., 2000, *MNRAS*, **314**, 475
- Barnes J., Hut P., 1986, *Nature*, **324**, 446
- Behroozi P. S., Wechsler R. H., Conroy C., 2013, *ApJ*, **770**, 57
- Bergström L., Edsjö J., Gondolo P., Ullio P., 1999, *Phys. Rev. D*, **59**, 043506
- Bose S., et al., 2016, preprint, ([arXiv:1604.07409](#))
- Brainerd T. G., Goldberg D. M., Verner Villumsen J., 1998, *ApJ*, **502**, 505
- Brooks A. M., Zolotov A., 2014, *ApJ*, **786**, 87
- Bryan G. L., Norman M. L., 1998, *ApJ*, **495**, 80
- Bullock J. S., Boylan-Kolchin M., 2017, preprint, ([arXiv:1707.04256](#))
- Campbell D., van den Bosch F. C., Padmanabhan N., Mao Y.-Y., Zentner A. R., Lange J. U., Jiang F., Villarréal A., 2017, preprint, ([arXiv:1705.06347](#))
- Carlberg R. G., 1994, *ApJ*, **433**, 468
- Choi J.-H., Weinberg M. D., Katz N., 2007, *MNRAS*, **381**, 987
- Choi J.-H., Weinberg M. D., Katz N., 2009, *MNRAS*, **400**, 1247
- Colín P., Avila-Reese V., González-Samaniego A., Velázquez H., 2015, *ApJ*, **803**, 28
- Conroy C., Wechsler R. H., Kravtsov A. V., 2006, *ApJ*, **647**, 201
- Dehnen W., 2001, *MNRAS*, **324**, 273
- Dehnen W., Read J. I., 2011, *European Physical Journal Plus*, **126**, 55
- Despali G., Vegetti S., 2016, preprint, ([arXiv:1608.06938](#))
- Diemand J., Moore B., Stadel J., Kazantzidis S., 2004a, *MNRAS*, **348**, 977
- Diemand J., Moore B., Stadel J., 2004b, *MNRAS*, **352**, 535
- Diemand J., Kuhlen M., Madau P., 2007a, *ApJ*, **657**, 262
- Diemand J., Kuhlen M., Madau P., 2007b, *ApJ*, **667**, 859
- Dolag K., Borgani S., Murante G., Springel V., 2009, *MNRAS*, **399**, 497
- Dutton A. A., Macciò A. V., 2014, *MNRAS*, **441**, 3359
- Eddington A. S., 1916, *MNRAS*, **76**, 572
- Fellhauer M., Lin D. N. C., 2007, *MNRAS*, **375**, 604
- Fiacconi D., Madau P., Potter D., Stadel J., 2016, *ApJ*, **824**, 144
- Frenk C. S., White S. D. M., Davis M., Efstathiou G., 1988, *ApJ*, **327**, 507
- Fujii M., Funato Y., Makino J., 2006, *PASJ*, **58**, 743
- Gao L., White S. D. M., Jenkins A., Stoeckl F., Springel V., 2004, *MNRAS*, **355**, 819
- Garrison-Kimmel S., et al., 2017, preprint, ([arXiv:1701.03792](#))
- Ghigna S., Moore B., Governato F., Lake G., Quinn T., Stadel J., 1998, *MNRAS*, **300**, 146
- Giocoli C., Tormen G., van den Bosch F. C., 2008a, *MNRAS*, **386**, 2135
- Giocoli C., Pieri L., Tormen G., 2008b, *MNRAS*, **387**, 689
- Giocoli C., Tormen G., Sheth R. K., van den Bosch F. C., 2010, *MNRAS*, **404**, 502
- Goerdt T., Gnedin O. Y., Moore B., Diemand J., Stadel J., 2007, *MNRAS*, **375**, 191
- Griffen B. F., Ji A. P., Dooley G. A., Gómez F. A., Vogelsberger M., O’Shea B. W., Frebel A., 2016, *ApJ*, **818**, 10
- Guo Q., White S., 2013, *ArXiv:1303.3586*,
- Guo Q., White S., Li C., Boylan-Kolchin M., 2010, *MNRAS*, **404**, 1111
- Han J., Jing Y. P., Wang H., Wang W., 2012, *MNRAS*, **427**, 2437
- Han J., Cole S., Frenk C. S., Jing Y., 2016, *MNRAS*, **457**, 1208
- Han J., Cole S., Frenk C. S., Benítez-Llambay A., Helly J., 2017, preprint, ([arXiv:1708.03646](#))
- Hayashi E., Navarro J. F., Taylor J. E., Stadel J., Quinn T., 2003, *ApJ*, **584**, 541
- Hearin A. P., Zentner A. R., Berlind A. A., Newman J. A., 2013, *MNRAS*, **433**, 659
- Hearin A. P., Watson D. F., van den Bosch F. C., 2015, *MNRAS*, **452**, 1958
- Hearin A. P., Zentner A. R., van den Bosch F. C., Campbell D., Tollerud E., 2016, *MNRAS*, **460**, 2552
- Hernquist L., 1993, *ApJS*, **86**, 389
- Hobbs A., Read J. I., Agertz O., Iannuzzi F., Power C., 2016, *MNRAS*, **458**, 468
- Iannuzzi F., Dolag K., 2011, *MNRAS*, **417**, 2846
- Jiang F., van den Bosch F. C., 2016a, preprint, ([arXiv:1610.02399](#))
- Jiang F., van den Bosch F. C., 2016b, *MNRAS*, **458**, 2848
- Jiang L., Cole S., Sawala T., Frenk C. S., 2015, *MNRAS*, **448**, 1674
- Kang X., Jing Y. P., Mo H. J., Börner G., 2005, *ApJ*, **631**, 21
- Kazantzidis S., Moore B., Mayer L., 2004a, in Prada F., Martínez Delgado D., Mahoney T. J., eds, *Astronomical Society of the Pacific Conference Series Vol. 327, Satellites and Tidal Streams*. p. 155 ([arXiv:astro-ph/0307362](#))
- Kazantzidis S., Magorrian J., Moore B., 2004b, *ApJ*, **601**, 37
- Khochfar S., Burkert A., 2006, *A&A*, **445**, 403
- Kitzbichler M. G., White S. D. M., 2008, *MNRAS*, **391**, 1489
- Klypin A., Gottlöber S., Kravtsov A. V., Khokhlov A. M., 1999a, *ApJ*, **516**, 530
- Klypin A., Kravtsov A. V., Valenzuela O., Prada F., 1999b, *ApJ*, **522**, 82
- Klypin A. A., Trujillo-Gomez S., Primack J., 2011, *ApJ*, **740**, 102
- Knebe A., Arnold B., Power C., Gibson B. K., 2008, *MNRAS*, **386**, 1029
- Knebe A., et al., 2011, *MNRAS*, **415**, 2293

- Knebe A., et al., 2013, *MNRAS*, **435**, 1618
- Kravtsov A. V., Berlind A. A., Wechsler R. H., Klypin A. A., Gottlöber S., Allgood B., Primack J. R., 2004, *ApJ*, **609**, 35
- Kuhlen M., Diemand J., Madau P., 2008, *ApJ*, **686**, 262
- Kuijken K., Dubinski J., 1994, *MNRAS*, **269**, 13
- Lehmann B. V., Mao Y.-Y., Becker M. R., Skillman S. W., Wechsler R. H., 2015, preprint, ([arXiv:1510.05651](https://arxiv.org/abs/1510.05651))
- Lovell M. R., Frenk C. S., Eke V. R., Jenkins A., Gao L., Theuns T., 2014, *MNRAS*, **439**, 300
- Lu Z., Mo H. J., Lu Y., Katz N., Weinberg M. D., van den Bosch F. C., Yang X., 2014, *MNRAS*, **439**, 1294
- Macciò A. V., Moore B., Stadel J., Diemand J., 2006, *MNRAS*, **366**, 1529
- Marín F. A., Wechsler R. H., Frieman J. A., Nichol R. C., 2008, *ApJ*, **672**, 849
- Mayer L., Governato F., Colpi M., Moore B., Quinn T., Wadsley J., Stadel J., Lake G., 2001, *ApJ*, **559**, 754
- Mo H., van den Bosch F. C., White S., 2010, *Galaxy Formation and Evolution*. Cambridge University Press
- Moliné Á., Sánchez-Conde M. A., Palomares-Ruiz S., Prada F., 2016, preprint, ([arXiv:1603.04057](https://arxiv.org/abs/1603.04057))
- Moore B., Katz N., Lake G., 1996, *ApJ*, **457**, 455
- Moore B., Governato F., Quinn T., Stadel J., Lake G., 1998, *ApJ*, **499**, L5
- Moore B., Ghigna S., Governato F., Lake G., Quinn T., Stadel J., Tozzi P., 1999, *ApJ*, **524**, L19
- Moster B. P., Somerville R. S., Maubetsch C., van den Bosch F. C., Macciò A. V., Naab T., Oser L., 2010, *ApJ*, **710**, 903
- Moster B. P., Naab T., White S. D. M., 2013, *MNRAS*, **428**, 3121
- Moster B. P., Naab T., White S. D. M., 2017, preprint, ([arXiv:1705.05373](https://arxiv.org/abs/1705.05373))
- Muldrew S. I., Pearce F. R., Power C., 2011, *MNRAS*, **410**, 2617
- Nakasato N., Ogiya G., Miki Y., Mori M., Nomoto K., 2012, preprint, ([arXiv:1206.1199](https://arxiv.org/abs/1206.1199))
- Navarro J. F., Frenk C. S., White S. D. M., 1997, *ApJ*, **490**, 493
- Neto A. F., et al., 2007, *MNRAS*, **381**, 1450
- Ogiya G., Mori M., Miki Y., Boku T., Nakasato N., 2013, in *Journal of Physics Conference Series*. p. 012014, doi:10.1088/1742-6596/454/1/012014
- Onions J., et al., 2012, *MNRAS*, **423**, 1200
- Peñarrubia J., Benson A. J., 2005, *MNRAS*, **364**, 977
- Peñarrubia J., Kroupa P., Boily C. M., 2002, *MNRAS*, **333**, 779
- Peñarrubia J., Benson A. J., Walker M. G., Gilmore G., McConnachie A. W., Mayer L., 2010, *MNRAS*, **406**, 1290
- Pieri L., Bertone G., Branchini E., 2008, *MNRAS*, **384**, 1627
- Power C., Navarro J. F., Jenkins A., Frenk C. S., White S. D. M., Springel V., Stadel J., Quinn T., 2003, *MNRAS*, **338**, 14
- Power C., Robotham A. S. G., Obreschkow D., Hobbs A., Lewis G. F., 2016, *MNRAS*, **462**, 474
- Press W. H., Teukolsky S. A., Vetterling W. T., Flannery B. P., 1992, *Numerical recipes in FORTRAN. The art of scientific computing*. Cambridge University Press
- Price D. J., Monaghan J. J., 2007, *MNRAS*, **374**, 1347
- Pujol A., et al., 2017, *MNRAS*, **469**, 749
- Pullen A. R., Benson A. J., Moustakas L. A., 2014, *ApJ*, **792**, 24
- Reddick R. M., Wechsler R. H., Tinker J. L., Behroozi P. S., 2013, *ApJ*, **771**, 30
- Reddick R. M., Tinker J. L., Wechsler R. H., Lu Y., 2014, *ApJ*, **783**, 118
- Rocha M., Peter A. H. G., Bullock J. S., Kaplinghat M., Garrison-Kimmel S., Oñorbe J., Moustakas L. A., 2013, *MNRAS*, **430**, 81
- Springel V., White S. D. M., 1999, *MNRAS*, **307**, 162
- Springel V., White S. D. M., Tormen G., Kauffmann G., 2001, *MNRAS*, **328**, 726
- Springel V., et al., 2005, *Nature*, **435**, 629
- Springel V., et al., 2008, *MNRAS*, **391**, 1685
- Strigari L. E., Koushiappas S. M., Bullock J. S., Kaplinghat M., 2007, *Phys. Rev. D*, **75**, 083526
- Taffoni G., Mayer L., Colpi M., Governato F., 2003, *MNRAS*, **341**, 434
- Taylor J., 1997, *Introduction to Error Analysis, the Study of Uncertainties in Physical Measurements*, 2nd Edition. University Science Books
- Taylor J. E., Babul A., 2001, *ApJ*, **559**, 716
- Tollet É., Cattaneo A., Mamon G., Moutard T., van den Bosch F., 2017, preprint, ([arXiv:1707.06264](https://arxiv.org/abs/1707.06264))
- Tormen G., 1997, *MNRAS*, **290**, 411
- Tormen G., Bouchet F. R., White S. D. M., 1997, *MNRAS*, **286**, 865
- Trujillo-Gomez S., Klypin A., Primack J., Romanowsky A. J., 2011, *ApJ*, **742**, 16
- Vale A., Ostriker J. P., 2004, *MNRAS*, **353**, 189
- Vogelsberger M., Zavala J., Loeb A., 2012, preprint, ([arXiv:1201.5892](https://arxiv.org/abs/1201.5892))
- Weinberg M. D., 1993, *ApJ*, **410**, 543
- Weinberg D. H., Colombi S., Davé R., Katz N., 2008, *ApJ*, **678**, 6
- Wetzel A. R., 2011, *MNRAS*, **412**, 49
- Wetzel A. R., Hopkins P. F., Kim J.-h., Faucher-Giguère C.-A., Kereš D., Quataert E., 2016, *ApJ*, **827**, L23
- Widrow L. M., 2000, *ApJS*, **131**, 39
- Zentner A. R., Berlind A. A., Bullock J. S., Kravtsov A. V., Wechsler R. H., 2005, *ApJ*, **624**, 505
- Zentner A. R., Hearin A. P., van den Bosch F. C., 2014, *MNRAS*, **443**, 3044
- Zentner A. R., Hearin A., van den Bosch F. C., Lange J. U., Villarreal A., 2016, preprint, ([arXiv:1606.07817](https://arxiv.org/abs/1606.07817))
- van Kampen E., 1995, *MNRAS*, **273**, 295
- van Kampen E., 2000, *ArXiv Astrophysics e-prints*, van den Bosch F. C., 2017, *MNRAS*, **468**, 885
- van den Bosch F. C., Jiang F., 2016, *MNRAS*, **458**, 2870
- van den Bosch F. C., Lewis G. F., Lake G., Stadel J., 1999, *ApJ*, **515**, 50
- van den Bosch F. C., Norberg P., Mo H. J., Yang X., 2004, *MNRAS*, **352**, 1302
- van den Bosch F. C., Tormen G., Giocoli C., 2005, *MNRAS*, **359**, 1029
- van den Bosch F. C., Ogiya G., Hahn O., Burkert A., 2017, in prep.

## APPENDIX A: DISCRETENESS NOISE IN THE SUBHALO MASS LOSS RATE

In §5 we discuss how discreteness noise gives rise to a runaway instability, in which the variance in  $f_{\text{bound}}(t)$  among many simulations, which only differ in their random realizations of the initial conditions, increases with time. We defined  $T_{\text{dis}}$  as the time when the standard deviation in  $f_{\text{bound}}$  among these simulations becomes 0.1 dex, and defined  $N_{\text{dis}}$  as the average number of bound particles in the subhalo at time  $T_{\text{dis}}$ . Here we derive a relation between  $N_{\text{dis}}$  and the number of particles,  $N_p$ , in the initial subhalo, assuming only that the discreteness noise obeys Poisson statistics.

Let  $\langle \Delta N \rangle$  be the expectation value for the number of particles that will be stripped off during a time interval  $\Delta t$ . We have that  $\langle \Delta N \rangle = \dot{m} \Delta t / m_p$ , where  $m_p$  is the particle mass, and  $\dot{m}$  is the system's instantaneous mass loss rate in the limit  $m_p \rightarrow 0$ . Due to sampling noise, there will be Poisson fluctuations in the actual  $\Delta N$ , and thus in the mass-loss rate in the numerical simulation. In particular, the typical error in  $\Delta N$  due to these Poisson fluctuations will be equal to  $\sigma_{\Delta N} = \sqrt{\langle \Delta N \rangle}$ . Clearly, the only way to suppress this



Poisson noise is to increase the number of particles that is used to model the subhalo.

Consider a system that, due to this Poisson noise, experiences a high fluctuation in the mass loss rate during a time step  $\Delta t$ , i.e.,  $\Delta N > \langle \Delta N \rangle$ . Subsequently, the system will re-virialize (roughly on a dynamical time) to adjust to this mass loss. Because the system in question experienced a higher-than-average episode of mass loss, it will also experience more significant re-virialization, which results in a more-than-average expansion of the remnant. Consequently, the system in question will be less dense than average, and hence experience more mass loss in the subsequent time interval; after all, less dense systems experience higher mass loss rates. Hence, the fluctuations in  $\Delta N$  in different time-intervals  $\Delta t$  are going to be positively correlated, which implies that the numerical error in the time-evolution of the subhalo mass,  $m(t)$ , will grow with time; i.e., *discreteness noise in a tidal field results in a run-away instability*.

Here we use a simple toy model to estimate at what  $N$  this problem becomes appreciable. If we define ‘appreciable’ as corresponding to a situation in which a  $1\sigma$  fluctuation in  $\Delta N$  (during a time-interval  $\Delta t$ ) implies a fluctuation in the corresponding mass-loss-rate of 10 percent, then we have that the problem becomes appreciable if  $\langle \Delta N \rangle = 100$ . The relevant time-scale  $\Delta t$  is the time-scale on which the subhalo re-arranges its mass distribution in response to the mass loss, which is of order the dynamical time,  $\tau_{\text{dyn}}$ , of the subhalo remnant. Hence, we argue that the Poisson fluctuations become appreciable once the expectation value for the mass loss rate becomes of order 100 particles per subhalo dynamical time.

Jiang & van den Bosch (2016b) have shown that the *average* subhalo mass loss rate (averaged over all orbits and orbital phases) in numerical simulations is such that, to good approximation,

$$m(t + \Delta t) = m(t) \exp(-\Delta t / \tau_{\text{strip}}), \quad (\text{A1})$$

where  $\tau_{\text{strip}}$  is a characteristic time scale for mass loss. Using this relation, we find that a subhalo loses on average 100 particles per dynamical time if its instantaneous number of particles is

$$N = \frac{100}{1 - \exp[-\tau_{\text{dyn}} / \tau_{\text{strip}}]}. \quad (\text{A2})$$

Using that the dynamical time is proportional to the crossing time,

$$t_{\text{cross}} \equiv \sqrt{\frac{2 r_{\text{h}}^3}{G m(t)}} \quad (\text{A3})$$

with  $r_{\text{h}}$  the subhalo’s half-mass radius, and  $m(t)$  the bound mass of the subhalo at time  $t$ , we have that

$$\tau_{\text{dyn}}(t) \propto t_{\text{cross},0} \left[ \frac{(r_{\text{h}}/r_{\text{h},0})^3}{f_{\text{bound}}} \right]^{1/2}, \quad (\text{A4})$$

where a subscript 0 refers to the initial property of the subhalo, i.e., prior to being exposed to an external tidal field. In the case of cosmological simulations, this roughly coincides with the properties of the subhalo at the time of accretion into the host halo.

As discussed in §6.1, our simulations reveal a reasonably tight relation between  $f_{\text{bound}}$  and  $r_{\text{h}}/r_{\text{h},0}$  of the form

$r_{\text{h}}/r_{\text{h},0} \propto f_{\text{bound}}^{0.5}$ , independent of the subhalo’s orbit. Substituting this in Eq. A4, we can rewrite Eq. A2 as

$$N = \frac{100}{1 - \exp[-\alpha f_{\text{bound}}^{0.25}]}, \quad (\text{A5})$$

where  $\alpha \propto (\tau_{\text{dyn},0}/\tau_{\text{strip}})$  is a unitless parameter. Taylor expanding Eq. (A5) to first order yields that  $N \propto f_{\text{bound}}^{-0.25}$ . If we assume that this instantaneous number of particles is proportional to  $N_{\text{dis}}$ , then, using that  $f_{\text{bound}} = N/N_{\text{p}}$ , we finally obtain that  $N_{\text{dis}} \propto N_{\text{p}}^{0.2}$ . As discussed in §6.2, this is exactly the behavior seen in our simulation data (cf. Fig. 13).